
Article:
Gong, P. orcid.org/0000-0001-6352-1696, Leong, Z. orcid.org/0000-0002-7581-1276, Qi, J. orcid.org/0000-0001-5235-0027 et al. (9 more authors) (2023) Composition and phase structure dependence of magnetic properties for Co2FeCr0.5Alx (x=0.9, 1.2) multi principal component alloys. Acta Materialia, 256. 119113. ISSN 1359-6454

https://doi.org/10.1016/j.actamat.2023.119113

Acta Materialia 256 (2023) 119113

Contents lists available at ScienceDirect

Acta Materialia

journal homepage: www.elsevier.com/locate/actamat

Composition and phase structure dependence of magnetic properties for $Co_2FeCr_{0.5}Al_x$ (x=0.9, 1.2) multi principal component alloys

Peng Gong [a,*], Zhaoyuan Leong [b], Jiahui Qi [b], Thomas W J Kwok [c,d], John Nutter [b], Yunus Azakli [b], Lei Zhou [e], Roberto Palacin [a], Claire Davis [e], Russell Goodall [b], Nicola Morley [b], W. Mark Rainforth [b,*]

[a] School of Engineering, Newcastle University, Newcastle upon Tyne, Newcastle NE1 7RU, UK
[b] Department of Materials Science and Engineering, University of Sheffield, Sir Robert Hadfield Building, Mappin Street, Sheffield S1 3JD, UK
[c] Department of Materials, Imperial College London, Prince Consort Road, London SW7 2BP, UK
[d] Singapore Institute of Manfacturing Technology (SIMTech), Agency for Science Technology and Research, 5 Cleantech Loop 636732, Singapore
[e] WMG, International Manufacturing Centre, University of Warwick, Coventry CV4 7AL, UK

ARTICLE INFO

Keywords:
Multi-principal element alloys (MPEAs)
Microscale and nanoscale particles
Soft magnetic properties

ABSTRACT

This article investigates the microstructure evolution, phase formation, and magnetic properties of $Co_2FeCr_{0.5}Al_x$ (x = 0.9, 1.2) complex component alloys, as a function of heat treatment temperatures (at 500, 600, 700, and 1150°C), using XRD, optical microscopy, electron microscopy and vibrating sample magnetometry (VSM). The alloy with 20.4 at% Al (x= 0.9), identified here as C1, consisted of microscale BCC1 phase and BCC nanoscale particles containing mainly Fe and Cr, and B2 matrix with mainly Al and Co. Partial transformation of the BCC1 phase to an FCC phase was observed at 700°C and full transformation at 1150°C, through twinning. For the sample with 25.5 at% Al (x= 1.2), identified as sample C2, there were only nanoscale BCC particles in the B2 matrix with the same element segregation between the phases as C1. This increase in Al (from x= 0.9 to 1.2) content stabilised the B2 matrix phase, reduced the grain size, and increased both saturation magnetisation (M_s) and coercivity (H_c). Moreover, increasing the heat treatment temperature resulted in an increase in grain size of the B2 matrix, volume fraction and average size of the micro BCC 1 and nanoscale BCC phases for both C1 and C2, which also modified the soft magnetic properties, with M_s and H_c increasing up to 600°C followed by a decrease until 1150°C. Using the structural information as inputs for density functional theory calculations of H_c and M_s, it has been found that the H_c is influenced by the grain size of the matrix, and the volume fraction and size of the BCC1 phase at temperature higher than 600°C for C1 and 700°C for C2, but is controlled by nanoscale BCC particles below these temperatures. The M_s is controlled by the elemental diffusion and segregation. Thus, the best combination of H_c and M_s was seen with antiferromagnetic Cr segregated and partitioning in the microscale BCC1 phase, and a B2 matrix with less Cr rich precipitation, formed at 500°C, where the misfit strain between B2 matrix and nanoscale BCC was low.

1. Introduction

A key global priority for the environment is to progress to zero carbon emissions as soon as possible. Central to this endeavour is a combination of electrification of many industrial sectors currently reliant on non-renewable energy, and the adoption of zero-carbon sources of electricity from wind, solar, nuclear, and fuel cells [1,2]. Electrical machines are at the heart of the electrification of many types of transport and industry sectors with continual demands for improvements in performance as set out in key industry roadmaps, for example, for the automotive [3,4] and aerospace [5–7] sectors. Due to the higher speed and higher efficiency requirements in commercial markets with lower energy loss, there is a need to develop the next generation of superior performance electrical machines [8–10]. However, one of the limitations for high performance and high-speed electrical machines is their high core loss, due to the soft magnetic materials currently used [11,12]. Existing soft magnetic materials, such as electrical steels and Co-Fe, have excellent saturation magnetic flux density (B_s), which is up to 2.0T with a coercivity (H_c) of 40 A/m for electrical steels [13,14], and B_s up to 2.4T and coercivity (H_c) of 60-100 A/m for Co-Fe[15]. However, they have

* Corresponding authors.

https://doi.org/10.1016/j.actamat.2023.119113
Received 2 April 2023; Received in revised form 16 June 2023; Accepted 25 June 2023
Available online 29 June 2023

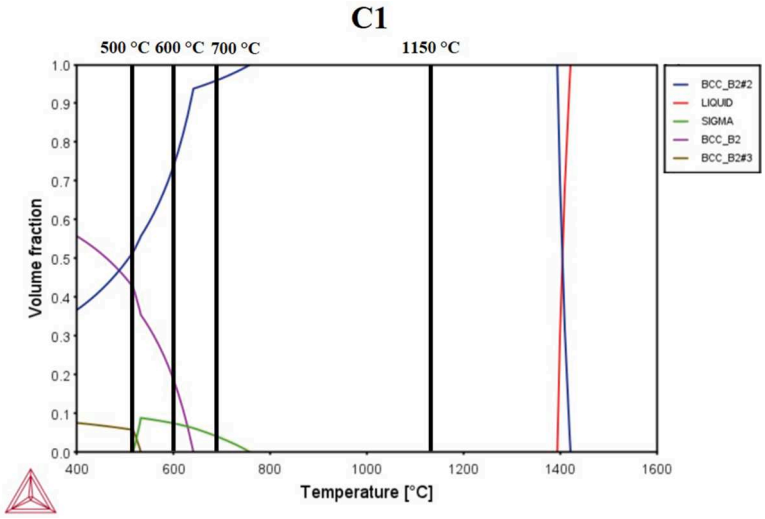

Fig. 1. Thermo-Cacl predicted temperature vs. phase fraction phase diagram for C1, including selected ageing temperatures.

been restricted by their low electrical resistivity, which is around 40×10^{-8} Ωm; this accounts for up to 60% of the core loss in high-speed electrical machines, as eddy currents are induced in the core, causing heating [16–18].

Multi principal-element alloys (MPEAs), consisting of elements with equimolar or non-equimolar mixing (also known as High Entropy Alloys (HEAs)), have been reported showing excellent mechanical properties, such as high strength, good room temperature ductility, good resistance to wear, along with high thermal stability, and high electrical resistivity [19–23]. MPEs containing 3d transition metal elements, such as Fe, Cu, Co, Ni, or Mn also show promising soft magnetic properties [23,24]. A series of FeCoNi based HEA with excellent mechanical properties and promising ferromagnetic properties have been developed in recent years, such as FeCoNi(AlSi)x with Bs to 1.15T, and Hc to 1400 A/m [25], and FeCoNi(CrAl)x with Ms to 13-64 emu/g and Hc to 1416 A/m [26]. Yeh et al.[27] and Wang et al. [28] also observe that, with increasing Al content in AlxCoCrFeNi alloys, the microstructure will transform from FCC to FCC+BCC structure (0.5<x<0.9), and then to full BCC structure, which consequently changes H_c, due to the different lattice barriers for domain wall mobility.

The utilization of MPEAs as potential soft magnetic materials in electrical machines has been hindered by their low B_s [29] and high H_c [22]. Based on prior research, the rules have been developed that ferromagnetic elements mainly control the B_s [19,30], and aspects of the microstructure, such as grain size or second phase, control the H_c [31–33], which clearly guides the design of new MPEAs [34,35]. Recent research has shown that multi-phase microstructures are more likely to exhibit excellent soft magnetic properties compared to single-phase solid solutions, as the coherent nanoscale precipitation can be used to render these alloys with better high temperature microstructural stabilities [19]. For example, Ma et al. [36] reported that nanoscale BCC precipitates (3-7 nm) uniformly distributed in a B2 phase matrix significantly reduce the coercivity of a MPEA to 127.3 A/m, as these precipitates effectively reduce the internal stress wavelength by reducing the distance between two adjacent BCC particles from micro-scale cells. Han et al. [37] report that in $Fe_{32.6}Ni_{27.7}Co_{27.7}Ta_{5.0}Al_{7.0}$, an $L1_2$ phase is precipitated in an FCC matrix, which, if controlled to a particle size of 91nm, gives extremely low coercivity as the coherent particles are below the domain wall size, but large enough to reduce coherency strains over very small particles. The saturation magnetisation of this latter alloy is however moderate, likely due to the FCC matrix structure.

Although the above-mentioned work has demonstrated the great potential of MPEAs in soft magnetic applications, key scientific questions have remained unanswered. For instance, in the alloys explored so far the impact of elemental partitioning and segregation between matrix and nanoscale BCC phases on the soft magnetic properties have not been analysed [38–40]. Furthermore, the effect of second phase evolution as a function of temperature on these properties is also unknown. For example, it is widely recognized that only coherent precipitates, in a specific size range, within either a fully B2 or FCC matrix, can improve the soft magnetic properties. But there is no investigation into how microscale particles and phase transformation during heat treatment influence soft magnetic properties. We seek to address this here. Since Al has a strong influence on the phase constitution, and can promote a change from FCC to BCC [41], we investigate the non-equiatomic MPEAs $Co_2FeCr_{0.5}Al_x$ (x = 0.9 and 1.2) with different second phase consititution. The heat treatment temperatures to alter the phase structure, were selected according to Thermo-Calc calculations. This should generate samples with different phase make-up and allow measurement of the change in B_s and H_c. This knowledge will help guide alloy design, providing desirable microstructures for the improved magnetic properties.

2. Alloy design rationale and heat treatment temperature selection

The magnetic strain theory indicates that the coercivity (H_c) depends on the energy required to displace domain walls, which led the current research to focus on developing nanoscale particles. Ma et al. [36] designed a new MPEA in the AlCoFeCr system with an Al:(Co+Cr) ratio from 0.2 to 0.45, where ferromagnetic BCC nanoprecipitates were present in the B2 matrix, which enhanced the stability of the nanoscale particles and improved the coercivity, with a maximum value at a ratio of 0.2.

Morley et al. [42] investigated Al-containing CoCrFeNi compositions with Al:(Co+Cr) ratios ranging from 0 to 1.0, with maximum saturation magnetisation achieved at 0.6. This was attributed to elemental partitioning resulting in a higher concentration of nanoscale particles, which enhance the total average magnetic moment per formula unit and leads to a higher M_s.

Following on from this work, we adopted the AlCoFeCr system for our study, but varied the Al:(Co+Cr) ratio within the range of 0.2 and 0.6 to achieve a balance performance in terms of Hc and Ms. In accordance with this objective, we have developed two alloys: $Co_2FeCr_{0.5}Al_{0.9}$ and $Co_2FeCr_{0.5}Al_{1.2}$ with Al:(Co+Cr) ratios of 0.36 and 0.48, respectively.

We use heat treatment to control elemental partitioning and

Table 1
Chemical compositions of the designed $Co_2FeCr_{0.5}Al_x$ alloys.

Co2FeCr0.5Alx	Co (at.%)	Fe (at.%)	Cr (at.%)	Al (at.%)
C1 (x=0.9)	45.5	22.7	11.4	20.4
C2 (x=1.2)	42.6	21.3	10.6	25.5

Table 2
Sample nomenclature corresponding to heat treatment for alloys C1 and C2.

Temperature (°C)	C1	C2
500	C1-1	C2-1
600	C1-2	C2-2
700	C1-3	C2-3
1150	C1-4	C2-4

nanoprecipitate/matrix formation to determine how the second phase influences the H_c. To inform the phase relationships of the designed MPEA, we utilized the computational thermodynamic software, Thermo-Calc™, with the TCHEA2 high entropy alloy v2.1.1 database, to generate phase diagram for $Co_2FeCr_{0.5}Al_{0.9}$ and $Co_2FeCr_{0.5}Al_{1.2}$, shown in Fig. 1. When the heat treatment exceeds 800°C, only the B2 matrix is present. At temperature between 600-800°C, the sigma phase forms, while a temperature lower than 650°C, lead to the achievement of the BCC phase. Reducing the temperature to 500°C results in the presence of three different BCC/B2 phases, with the sigma phase disappearing. Based on the Thermocalc™ calculations, we selected four heat treatment temperatures were chosen at 500°C, 600°C, 700°C and 1150°C.

This experimental design will produce materials with varying phase compositions, which enables us to measure changes in Ms (saturation magnetization) and Hc (coercivity). This knowledge will help guide alloy design, providing desirable microstructures for the improved magnetic properties.

3. Experimental

3.1. Processing $Co_2FeCr_{0.5}Al_x$ alloys

The measured compositions of the manufactured $Co_2FeCr_{0.5}Al_x$ (x=0.9, 1.2) alloys investigated in this study are listed in Table 1. Both alloys were produced from elemental feedstock with a purity of 99.9%. Alloys were manufactured as 12 mm diameter buttons with 8 mm thickness in an arc melting furnace with an argon atmosphere. The buttons were then homogenized at 1200°C for 2 hours followed by quenching in water to room temperature. Solidification of the given chemical compositions was explored by thermodynamic calculations using Thermo-Calc software with the TCHEA2 high entropy alloy v2.1.1 database, for prediction of equilibrium phase diagrams and phase transformation kinetics. The heat treatment temperatures for the alloys were then determined in relation to the phase transformation temperatures predicted; heat treatments were performed at 500°C, 600°C, 700°C and 1150°C for 24 hours, followed by water quenching. Table 2 outlines the sample nomenclature used here, relating to alloy compositions from Table 1 and the heat treatment temperatures. A schematic diagram showing the overall process route is given in Fig. 2. All heat treatments were undertaken in an Ar atmosphere in order to prevent oxidation.

3.2. Microstructure characterisation

Microstructural observations were performed by optical microscopy (OM), scanning electron microscopy (SEM), and transmission electron microscopy (TEM). Specimens for OM and SEM observation were prepared by standard metallographic methods, which included grinding from P400 to P1200 and polishing up to 0.04 μm colloidal silica particles. OM analysis was undertaken using a Nikon LV 150N and SEM using a FEI-Inspect F50 (20kV), respectively. Grain size analysis was undertaken using linear intercept analysis in two orthogonal directions to account for the elongated nature of the grains.

Thin specimens for TEM studies were prepared by FIB lift-out techniques, using a FEI-Helios dual-beam FIB. FIB lift-out was undertaken from specific sites to obtain the phase(s) of interest. TEM studies were conducted in a JEOL-F200 microscope operating at an accelerating voltage of 200 kV. The microstructural analyses were performed using both conventional diffraction contrast techniques with bright-field and dark-field images.

XRD measurements for phase analysis were performed on a Bruker D2 Advance diffractometer equipped with a Vantec position-sensitive detector and a graphite monochromator. Data was collected at room temperature using monochromatic Cu Kα radiation ($\lambda = 0.179026$ nm), 45 kV, 35 mA, in the 2θ region between 30° and 100°. The step size was 0.034° (2θ) and the counting time per step was 10s.

3.3. Measurement of magnetic properties

A Quantum Design MPMS-3 SQUID magnetometer was used to determine the magnetisation hysteresis loops and the field cooled (FC) magnetisation as a function of temperature and applied magnetic field. From the magnetisation hysteresis loops, the coercive field and saturation magnetisation were determined for each sample. The magnetic measurements were taken twice for each sample condition to check reproducibility. For the experimental step size, field measurements were taken on a log-step scale, to allow for more points around the low field region, compared to the high field region, where saturation occurs. Thus, between -3kA/m and 3kA/m the field step size was 0.5 kA/m or less. From the FC data, the Curie Temperatures were determined from the peak in the δM/δT vs T plots.

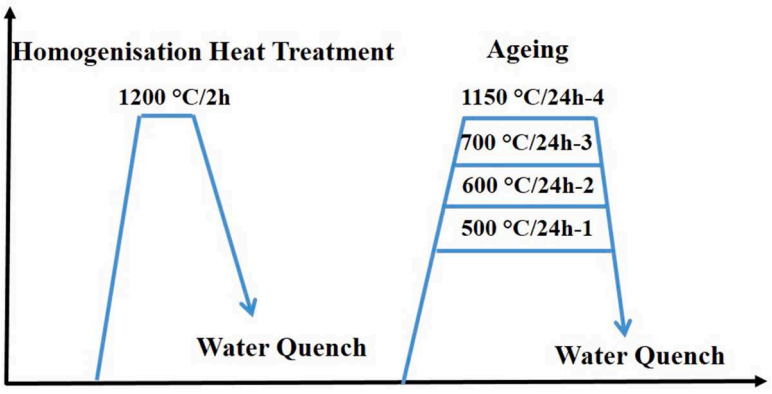

Fig. 2. Schematic of the thermomechanical cycles applied to the alloys.

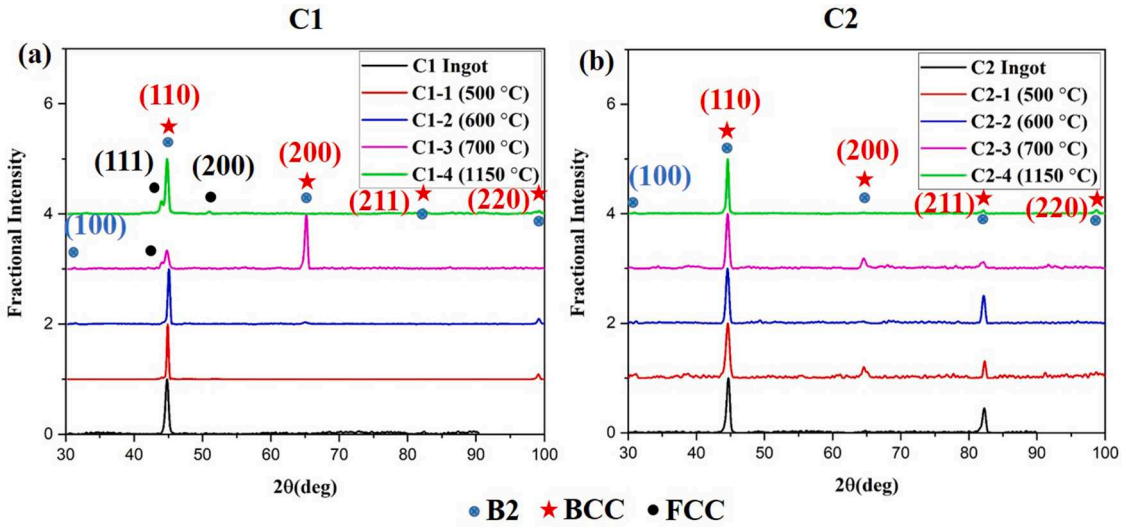

Fig. 3. XRD traces for the $Co_2FeCr_{0.5}Al_x$ MPEAs: (a) C1: $Co_2FeCr_{0.5}Al_{0.9}$; (b) C2: $Co_2FeCr_{0.5}Al_{1.2}$.

Table 3
Summary of the lattice parameters and FCC phase fraction (%) as a function of heat treatment temperature in C1 and C2 alloys, calculated from the X-ray.

Temperature (°C)	C1-$Co_2FeCr_{0.5}Al_{0.9}$				C2-$Co_2FeCr_{0.5}Al_{1.2}$	
	BCC: a (Å)	B2: a (Å)	FCC: a (Å)	FCC: wt(%)	BCC: a (Å)	B2: a (Å)
500	2.86	2.87	–	–	2.83	2.85
600	2.87	2.87	–	–	2.83	2.86
700	2.88	2.88	3.58	2	2.84	2.87
1150	–	2.90	3.65	18.9	2.86	2.88

4. Results

4.1. Crystal structures of $Co_2FeCr_{0.5}Al_x$ MPEAs

XRD patterns of the two alloy series (C1 and C2) are shown in Fig. 3 with BCC/B2 phase detected in the as-cast state, and after most heat treatments. FCC phase reflections appeared in the XRD patterns of C1-3 and C1-4, with a phase fraction of 2 % and 18.9 % respectively. The FCC phase was not predicted from the thermodynamic calculations, the reasons for which are discussed later. No FCC phase was detected in C2, which has a higher Al content, with only BCC/B2-based phases detected for the four different heat treatment temperatures. The lattice parameters of the BCC, B2 and FCC phases have been calculated and are listed in Table 3, with the lattice constant increasing with higher heat treatment temperature. The lattice spacing decreased with an increase in Al content, which is surprising [43,44], but as discussed later, the elemental composition of the phases changed overall such that the change in the Al content was not the only determining factor.

4.2. Microstructures of $Co_2FeCr_{0.5}Al_x$ MPEAs

4.2.1. Ingot microstructures

Optical Microscopy (OM) and SEM images of the ingot microstructures of the $Co_2FeCr_{0.5}Al_x$ alloys are shown in Fig. 4. For the C1 alloy, the OM and SEM images in Fig. 4 (a, b) showed contrast arising from the crystal orientation, but was otherwise uniform. The SEM-EDS indicated a uniform composition. XRD indicated a single BCC/B2 phase. For the C2 alloy, a fine dendritic microstructure was observed, Fig. 4 (c, d). SEM-EDS results indicated segregation of Al, Co and Cr on a coarser scale than the dendritic structure. The elemental segregation in C2, which was absent in C1, suggests a higher freezing range for the C2 alloy compared to C1.

4.2.2. Microstructure evolution as a function of heat treatment temperatures

Grain size and second phase volume fraction analysis by Optical Microscopy (OM) and SEM. The microstructure evolution of $Co_2FeCr_{0.5}Al_x$ alloys is shown in Fig. 5 for the C1 alloy and Fig. 6 for the C2 alloy as a function of four heat treatment temperatures. For the C1 alloy, the microscale BCC1 phase is clearly visible in XRD spectra at four different temperatures, with an acicular or needle morphology, exhibiting bright contrast compared to the B2 matrix. The volume fraction and the average size of the microscale BCC1 phase increased as a function of temperature, shown in Fig. 7 (b). The FCC phase was not visible in optical micrographs after heat treatment at 700°C and 1150°C, and therefore TEM was used, discussed in section 4.2.2.3. For the C2 alloy, only one phase was visible in optical micrographs, likely to be a BCC/B2-based phase, but again TEM was needed to confirm this. The average grain size has also been measured after heat treatment on C1 and C2 alloys, which increases with heat treatment temperature in both cases, shown in Fig. 7 (a). The C1 alloy has much larger grains than the C2 alloy at all four temperatures.

Elements distribution analysis by SEM-EDS. To analyse the elemental segregation and distribution, backscattered SEM images with EDS maps were taken and are shown in Figs. 8-11 for C1 and C2 alloys at heat treatment temperatures of 500°C and 1150°C. These two temperatures were selected for microstructural analysis by SEM, as according to the XRD and OM results, the alloys between 500°C and 700°C have similar phase constitution and structure. The microstructure of the heat treated C1 alloy observed by SEM is shown in Figs. 8 and 9, with the microscale BCC1 phase (light contrast) formed as angular particles in the B2 matrix and uniformly along the grain boundaries in the B2 matrix. As seen in the SEM-EDS maps in Figs. 8 (b-f) and 9 (b-f), Cr and Fe partition to the microscale BCC1 phase, whereas Al partitions to the B2 matrix, with Co homogenously distributed in the two phases for both heat treatment temperatures. For the C2 alloy, all elements are homogenously distributed in the B2 matrix with a minor amount of Cr segregated on the grain boundaries, presumably associated with microscale BCC1 phase, shown in Figs. 10 (b-f) and 11 (b-f).

Microscale and nanoscale second phase analysis by TEM. TEM analysis of C1 ($Co_2FeCr_{0.5}Al_{0.9}$) and C2 ($Co_2FeCr_{0.5}Al_{1.2}$) microstructural evolution

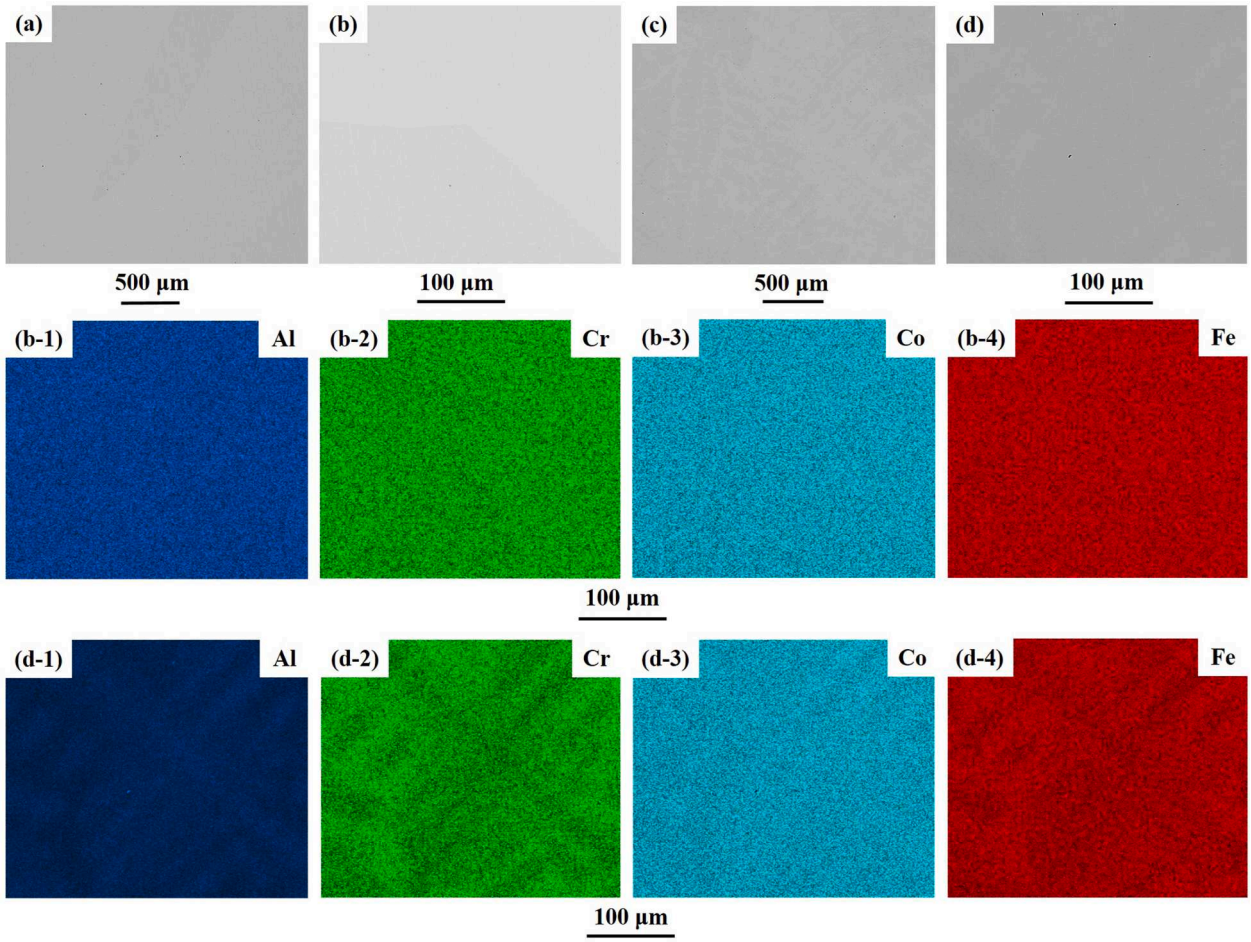

Fig. 4. OM, SEM and EDS images of C1: $Co_2FeCr_{0.5}Al_{0.9}$ and C2: $Co_2FeCr_{0.5}Al_{1.2}$ on ingot, C1 alloy (a) OM image, (b) SEM image and (b-1), (b-2), (b-3), (b-4) its corresponding EDS results on Al, Cr, Co and Fe; C2 alloy (c) OM image, (d) SEM image and (d-1), (d-2), (d-3), (d-4) its corresponding EDS results on Al, Cr, Co and Fe.

as a function of heat treatment at 500°C, 600°C, 700°C and 1150°C, is shown in Figs. 12-16 and Figs. 17-20, respectively. TEM samples were prepared using dual-beam FIB on the region with at least one or two microscale BCC1 phases for the C1 sample, and a random region for the C2 sample. For the C1 alloy, heat treated at 500°C and 600°C, there are similar microstructures with microscale BCC1 phase in the B2 matrix, shown in Figs. 12 and 13. With increasing magnification on the microscale BCC1 phase region in C1-1, as shown in Figs. 12 (b, c) there is only contrast arising from occasional dislocations. In contrast, in sample C1-2, dark contrast of stacking-faults can be seen in the bright-field STEM images, Fig. 13 (b, c). The $[110]_{BCC}$ (Fig. 12 (d)) in C1-1 and $[100]_{BCC}$ (Fig. 13 (b)) in C1-2 zone axis diffraction patterns from the microscale BCC1 phase, show weaker satellite spots in C1-1 and clear satellite spots in C1-2. The satellite spots are associated with stacking faults, which are clearly visible with darker contrast in the structure. No twinning is present. For the B2 matrix in C1 alloy at 500°C and 600°C, as shown in Figs. 12 (e-h) and 13 (c, d), including the corresponding $[110]_{BCC}$ zone axis diffraction pattern, there are spherical nanoscale BCC precipitates in ordered B2 matrix. In order to determine the chemical compositions of the three phases, STEM-EDS maps were acquired from those phases, with Cr and Fe concentration found in the microscale BCC1 phase and nanoscale BCC precipitates, and Al concentration in the B2 matrix, while the amount of Co remained constant, in Figs. 12 (j) and 13 (e, f).

Fig. 14 gives TEM images of the C1 alloy heat treated at 700°C. One microscale BCC1 phase was located in the B2 matrix, shown in Fig. 14 (a). There are two grains with different orientation in the BCC1 phase with different contrast in bright-field STEM images, shown in Fig. 14 (b) and (c). These were further identified by a selected area diffraction pattern with $[111]_{BCC}$ on the bottom grain in Fig. 14 (d)-1 and $[110]_{BCC}$ in the upper grain of Fig. 14 (d)-2. Both the bright-field image and diffraction pattern from microscale BCC1 phase show twinning, which contained stacking faults. The distribution of elements in the two phases have also been determined from interface between BCC1 and B2 matrix by STEM-EDS maps shown in Fig. 14 (e, f), with Cr and Fe concentration in the microscale BCC1 phase and nanoscale BCC particles, and Al concentration in matrix of B2, which are the same as the sample at 600°C, shown in Fig. 13 (f).

The matrix structures are still retained after heat treatment at 1150°C. However, as shown in the bright-field STEM images in Fig. 15 (b), with the corresponding selected area diffraction pattern, the microscale BCC1 phase has transformed from BCC to FCC crystal symmetry, which is consistent with the XRD data. The FCC phase contained numerous fine twins. Furthermore, the transformed FCC phase had the Kurdjumov-Sachs orientation relationship (OR) with the matrix, identified by the SADP in Fig. 15 (c), with $[111]_{BCC\text{-}matrix}//[011]_{FCC\text{-}second\ phase}$ and $\{110\}_{BCC\text{-}matrix}//\{111\}_{FCC\text{-}second\ phase}$. The elements segregated in the BCC1 and B2 phases are the same as observed in C1-1, C1-2 and C1-3, showing no change with increase in the heat treatment temperature, as shown by STEM-EDS maps in Fig. 15 (f). The BCC nanoscale precipitate disappeared in the B2 matrix, as shown by the diffraction pattern and EDS mapping in B2 region.

To directly understand the elemental partitioning and segregation between the B2-matrix and the microscale BCC1 phase (which is then partly transformed to an FCC phase as a function of heat treatment temperatures), the content of each element within each phase region, extracted from STEM-EDS maps, and how this varies after the different

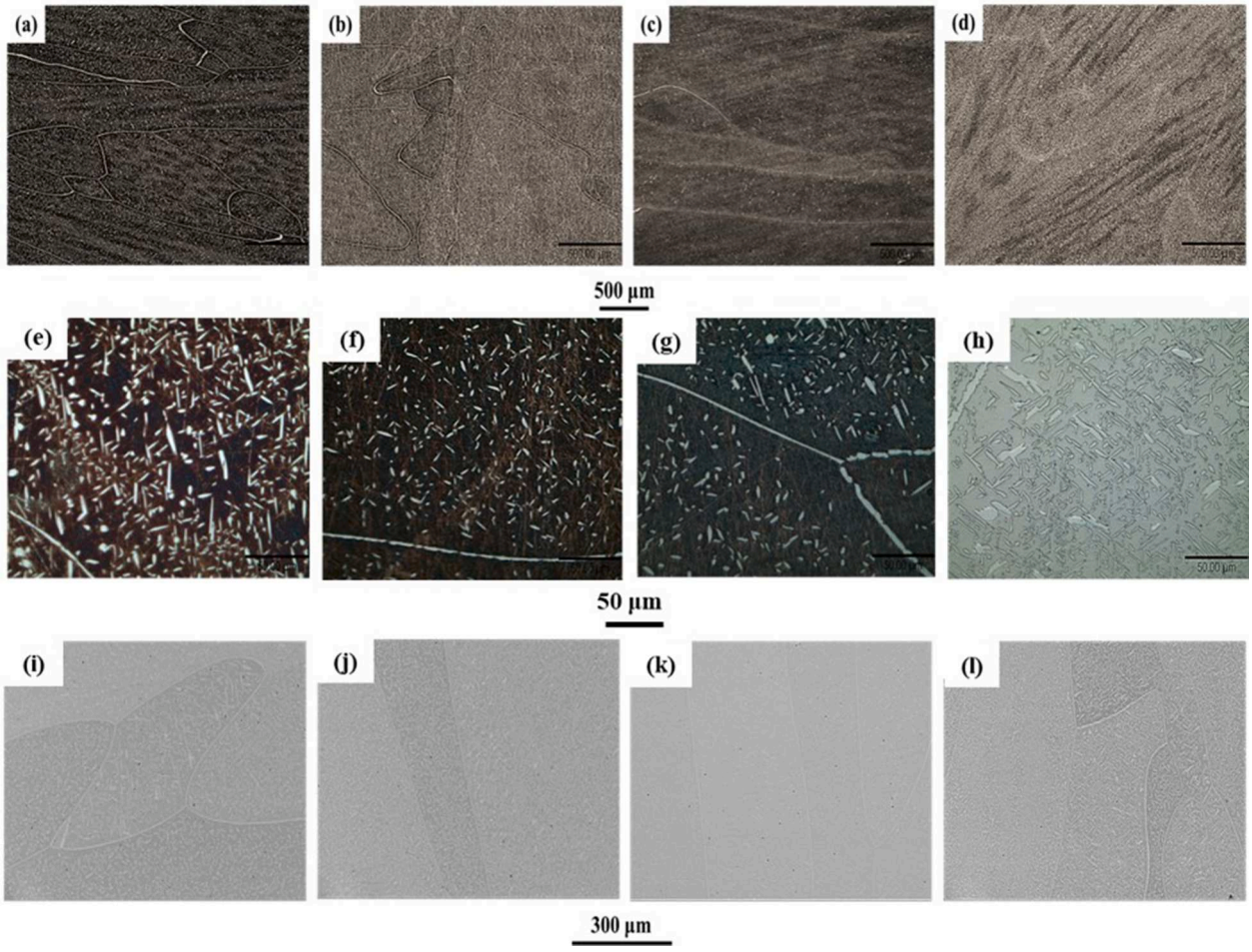

Fig. 5. OM and SEM images of C1: $Co_2FeCr_{0.5}Al_{0.9}$ at different heat treatment temperatures, (a), (e) and (i) C1-1; (b), (f) and (j) C1-2; (c), (g) and (k) C1-3; (d), (h) and (l) C1-4; with different magnifications of (a-h) OM and (i-l) SEM.

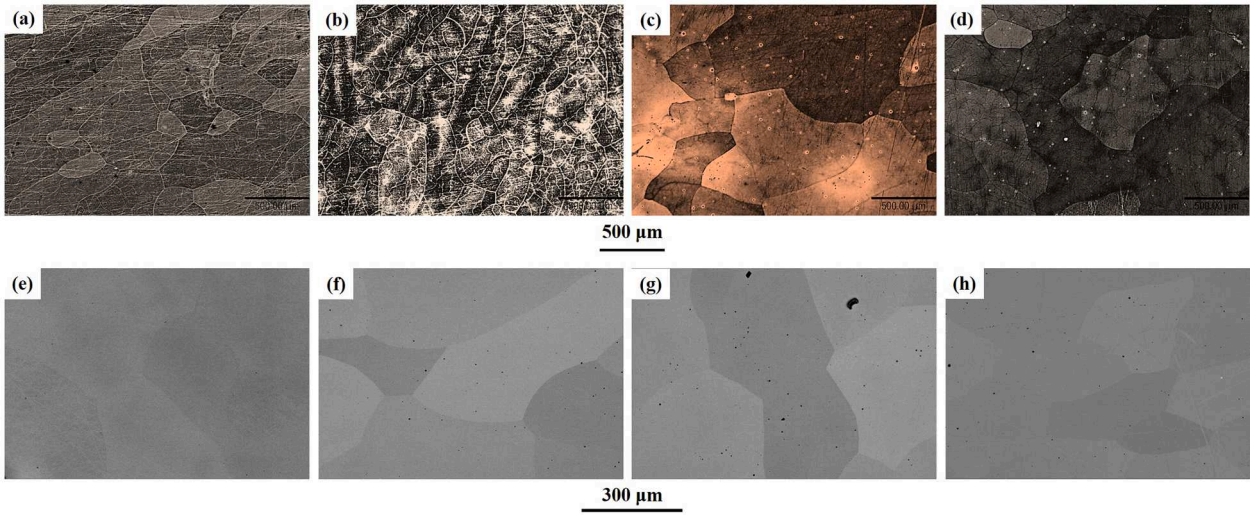

Fig. 6. OM and SEM images of C2: $Co_2FeCr_{0.5}Al_{1.2}$ at different heat treatment temperatures, (a) and (e) C2-1; (b) and (f) C2-2; (c) and (g) C2-3; (d) and (h) C2-4, with different magnifications of (a-d) OM and (e-h) SEM.

heat treatments, is shown in Fig. 16. The B2-matrix showed a relatively constant increase in Al concentration and a decrease in Cr concentration while comparatively the levels of Fe and Co are more constant. In contrast, the microscale BCC1 phase generally does not show a significant change in composition, although perhaps the Al concentration shows a small decrease with increase in temperature.

For the C2 alloy, the XRD, OM and SEM results indicate that there is only the B2 matrix and nanoscale precipitate BCC phase with no phase transformation to FCC during heat treatment at any of the four different temperatures. TEM images of C2-1, C2-2, C2-3 and C2-4 are shown in

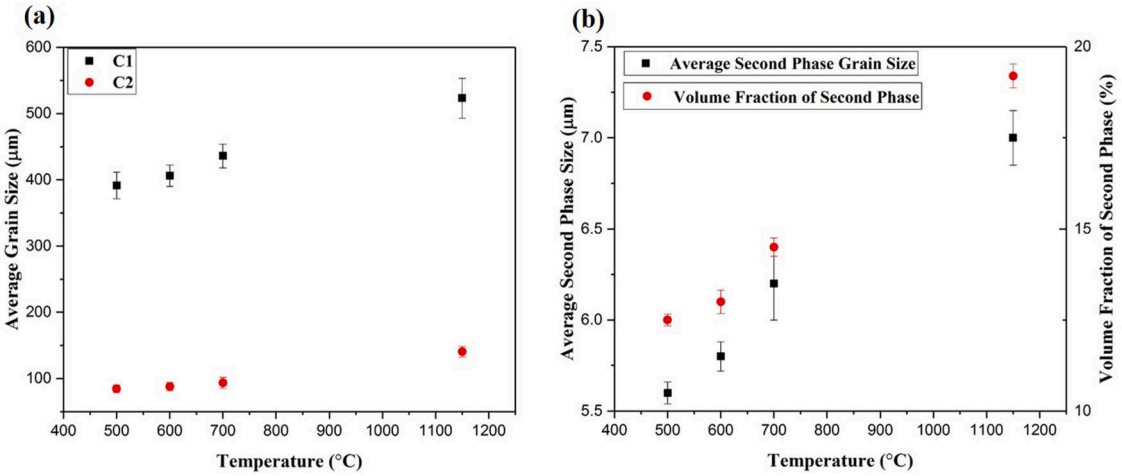

Fig. 7. (a) Average grain size of C1 and C2 alloys, and (b) average size and volume fraction of BCC1 in C1 alloy.

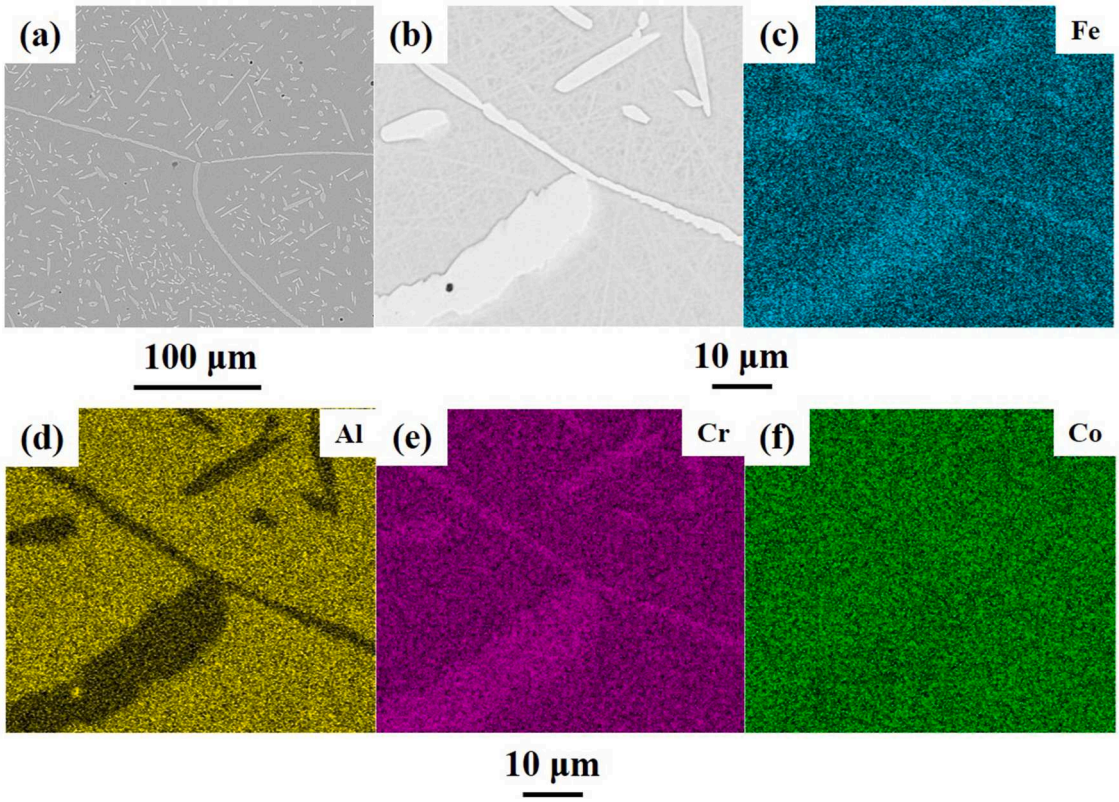

Fig. 8. SEM and EDS images of C1: $Co_2FeCr_{0.5}Al_{0.9}$ heat treated at 500°C, (a) SEM image at low magnification and (b-f) SEM images with its corresponding EDS results on Fe, Al, Cr and Co.

Figs. 17, 18. The ordered, spherical nanoscale BCC phase can be seen in the B2 matrix in the bright field images with phase confirmation by selected area diffraction patterns shown in Fig. 17. The elemental distribution has also been measured by STEM-EDX, shown as maps in Fig. 18. Cr is segregated to the nanoscale BCC particles, while Co, Al and Fe partition to the B2 matrix. The average diameter of the nanoscale BCC particles has also been measured, and is shown in Table 4, being 12.9 nm at 500°C, 16.7nm at 600°C, 25.2nm at 700°C, indicating coarsening with an increase in temperature. However, with heat treatment at 1150°C, most of the nanoscale BCC particles are dissolved into the B2 matrix, shown in Fig. 18 (h).

4.3. *Magnetic properties of $Co_2FeCr_{0.5}Al_x$*

An example magnetization (M) vs magnetic field intensity (H) curve is shown in Fig. 19, and the measured values of saturation magnetisation and coercivity are shown in Fig. 20. It is interesting to note that the addition of paramagnetic Al from x=0.9 in the C1 alloy to x=1.2 in the C2 alloy can lead to an increase in the saturation magnetization (M_s). This is because increasing Al can induce transformation from microscale BCC1+B2/nanoparticle BCC phase to B2+nanoparticle BCC phase. The heat treatment temperatures for both C1 and C2 alloys also influence the M_s. With increasing temperature, the M_s is initially increased to a maximum value of 119 Am^2/kg for C1 and 124 Am^2/kg for C2 at 600°C,

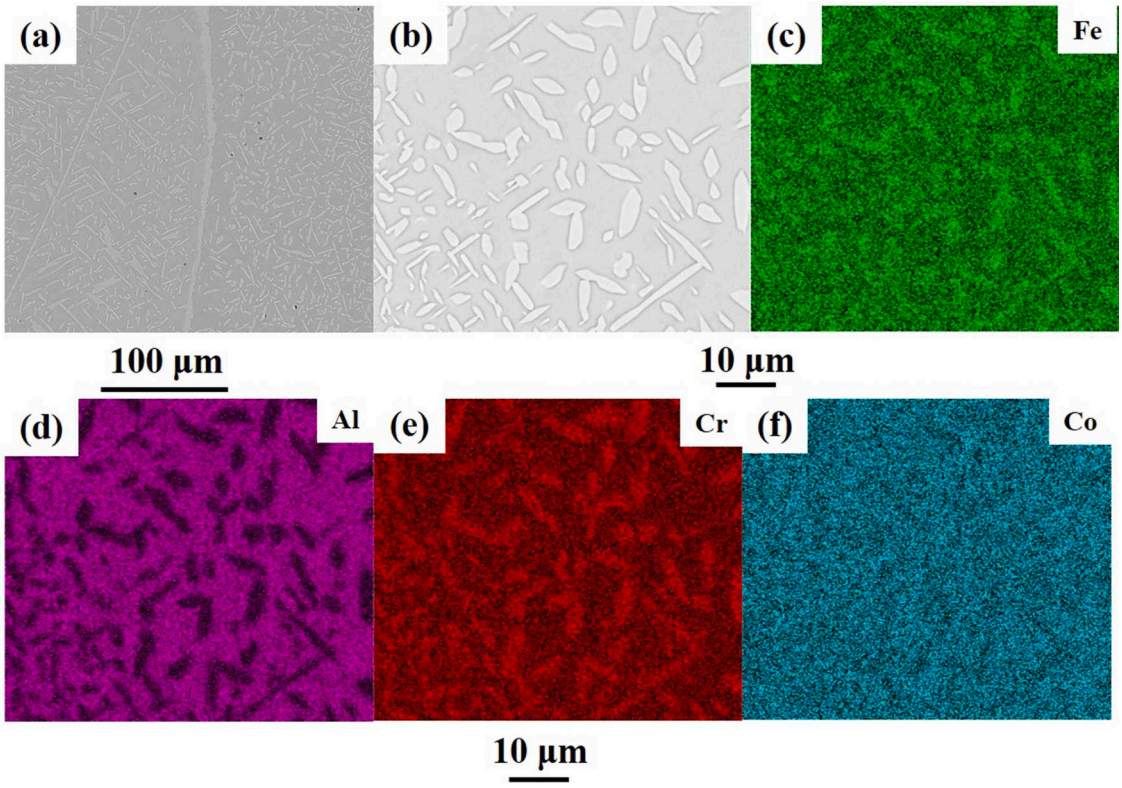

Fig. 9. SEM and EDS images of C1: $Co_2FeCr_{0.5}Al_{0.9}$ heat treated at 1150°C, (a) SEM image at low magnification and (b-f) SEM images with its corresponding EDS results on Fe, Al, Cr and Co.

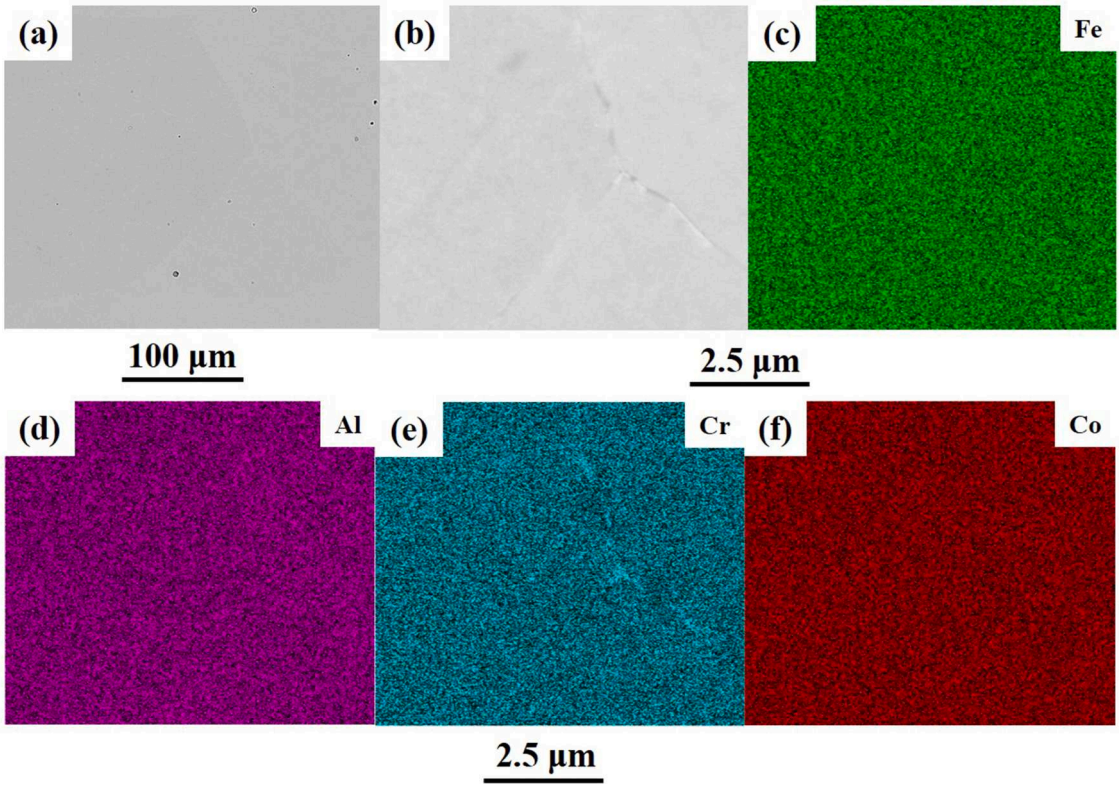

Fig. 10. SEM and EDS images of C2: $Co_2FeCr_{0.5}Al_{1.2}$ at 500°C, (a) SEM image at low magnification and (b-f) SEM images with its corresponding EDS results on Fe, Al, Cr and Co.

Table 4
Average diameter and volume fraction of nearly spherical BCC1 precipitates in C1 and C2 alloys.

Temp (°C)	Average size of nanoparticles (nm)		Volume fraction of nanoparticles (%)	
	C1	C2	C1	C2
500	12.6 nm	12.9 nm	12.5	10
600	15.2 nm	16.7 nm	13	27.4
700	18.9 nm	25.2 nm	14.3	33
1150	–	–	–	–

and then decreased, especially for C1 to 94 Am^2/kg at 1150°C. This is due to the transformation from BCC to FCC phase in the microscale second phase in the C1 alloy. The mixture of an ordered B2 and BCC phase was found to be ferromagnetic, and the FCC phase was non-magnetic or weakly ferromagnetic, which shows that the C1 alloy after heat treatment at 700°C and 1150°C does not exhibit a well-developed hysteresis in the M-H behaviour and has a very low saturation magnetization (M_s). However, the M_s for the C2 alloy also decreased from 600°C to 1150°C, which is more challenging to explain, this must have been a result of microstructural changes which will be discussed in the next section in relation to the TEM data.

Coercivity (H_c) values are higher in the C2 alloy than the C1 alloy, with higher content of Al, shown in Fig. 19 and Fig. 20 (b). The values are low at the initial heat treatment temperature of 500°C for both C1 and C2 alloys, and then start to increase to the maximum value of 1.62 kA/m at 600°C for the C1 alloy and 2.76 kA/m at 700°C for the C2 alloy, followed by a decrease to 0.82 kA/m at 1150°C for the C1 alloy and 2.53 kA/m at 1150°C for the C2 alloy. This result can be mainly explained by the change of the size of the relevant microstructural features in the C1 and C2 alloys, with larger grain size resulting in lower H_c. However, the smaller grain size at lower heat treatment temperature at 500°C induced lower H_c for both C1 and C2 alloys, which is due to the nanoscale particles in the B2 matrix, as will be discussed in the next section.

5. Discussion

5.1. Microstructure evolution and phase formation through diffusion, segregation and partitioning of elements

The phase diagram predicted using ThermoCalc-2018 software and the TCHEA2 high entropy alloy v2.1.1 database is shown in Fig. 21. For alloy compositions C1 and C2, the predicted phase diagram indicates only BCC/B2 phases nucleated from the liquid. Transformation on cooling is predicted to give three types of BCC/B2 phases at room temperature for C1 (Fig. 21 (a) black line) and C2 (Fig. 21 (c) black line), which are Co-Fe rich, Co-Al rich and Cr rich. For C1 and C2 alloys, the experimental results show the matrix is the Co-Al rich B2 phase, and Cr rich nanoscale particles are distributed in the B2 matrix. Moreover, for the C1 alloy, the second microscale BCC phase contains mainly Co-Fe-Cr, which transforms to the FCC phase after heat treatment at 700°C and 1150°C. For the C2 alloy, the Co-Fe rich BCC phase is not found. Thus, there are discrepancies between the experimental results and the thermodynamic calculations, especially for the C1 alloy where the FCC phase transformation occurs.

The microscale BCC1 phase in the C1 alloy has an Al content of 5-6 at %, according to the SEM-EDS data. Thermodynamic calculations suggest that, for this composition, the BCC1 should be fully FCC phase, which is predicted to be achieved only above 926°C, a maximum of 30% FCC phase above 676°C, and the full BCC/B2 phase below 676°C, where this should be the equilibrium phase to room temperature. These calculations are in good agreement with the experimental results, Fig. 3 and Table 3, with the microscale BCC1 phase fully transforming to FCC phase C1-4 at 1150°C, and partially becoming FCC from BCC1 in C1-3 at 700°C, and the microscale BCC1 phase remaining in C1-2 at 600°C and C1-1 at 500°C.

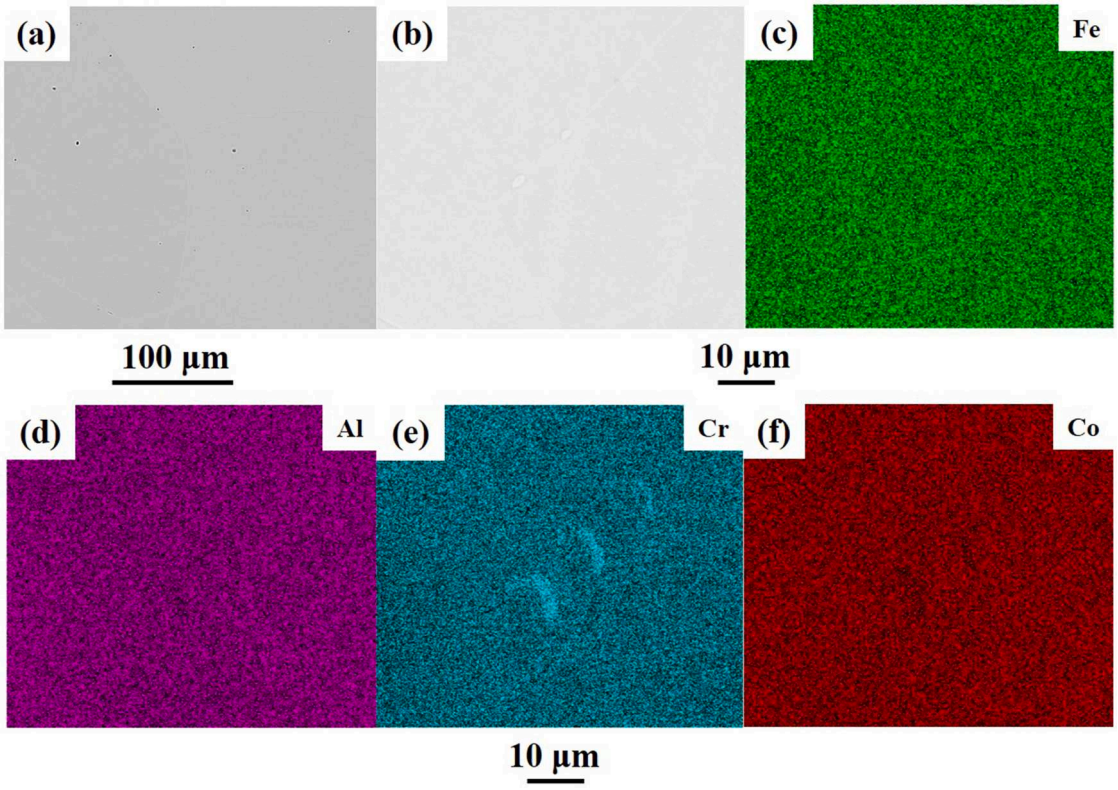

Fig. 11. SEM and EDS images of C2: $Co_2FeCr_{0.5}Al_{1.2}$ at 1150°C, (a) SEM image at low magnification and (b-f) SEM images with its corresponding EDS results on Fe, Al, Cr and Co (note in (e) there has been some specimen drift, artificially elongating the Cr distribution).

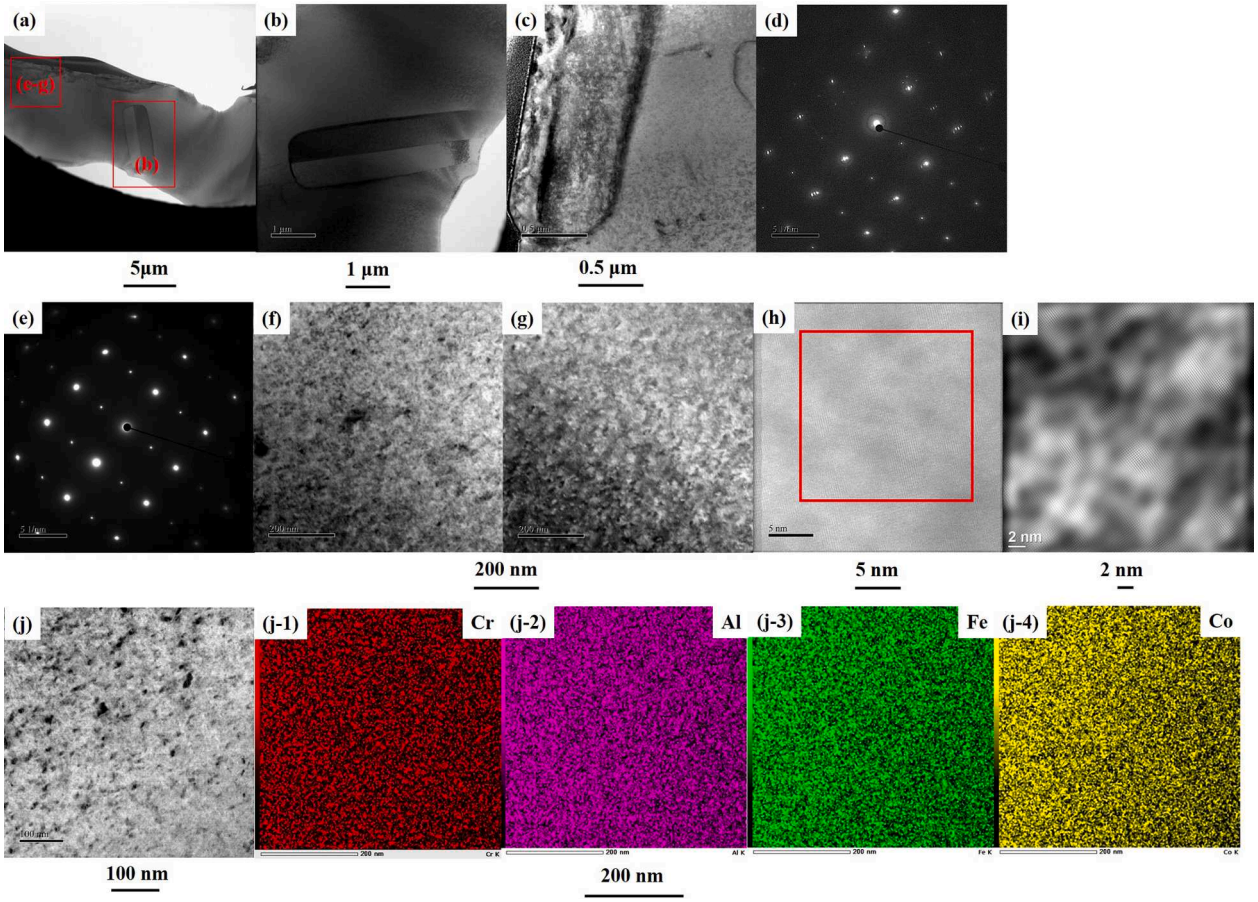

Fig. 12. STEM results from C1: $Co_2FeCr_{0.5}Al_{0.9}$ at 500°C, (a) low magnification bright-field STEM image showing microscale BCC1 phase (dark contrast) and B2 matrix; (b) and (c) high magnification bright-field STEM image from red rectangle in (a) shown microscale BCC1 phase; (d) selected area diffraction patterns from microscale BCC1 phase; (e) selected area diffraction patterns from B2 matrix; (f) Bright-field STEM image showing nanoscale BCC phase in the B2 matrix; (g) Dark-field STEM image corresponding to (f); (h) High resolution-TEM of the nanoscale BCC phase in B2 matrix; (i) FFT image from (h); (j) Bright-field STEM image on B2 matrix with its corresponding EDS maps of (j-1) Cr, (j-2) Al and (j-3) Fe, (j-4) Co.

For the experimental data, the XRD, OM SEM, and TEM results showed that in the C1 alloy, C1-1 and C1-2 consisted of microscale BCC1 and nanoscale BCC particles in a B2 matrix, with Fe+Cr+Co rich in the microscale BCC1, Cr rich in the nanoscale BCC, and Al+Co rich in B2 regions. Further increasing the temperature, the BCC1 phase transformed to the FCC phase with 2% of total phases in C1-3, and fully to the FCC phase with 18.9% of total phases in C1-4. Moreover, the microscale BCC1 average size and volume fraction increased with increasing heat treatment temperature, due to the more rapid diffusion of Cr and Fe from B2 into the microscale BCC1, shown in Fig. 6. Furthermore, for the Al+Co rich B2 phase, precipitation of a few ordered BCC phases nucleated at the Cr rich clusters, giving an increase in the volume fraction of the nanoscale BCC particles in C1-2 and C1-3. But in C1-4, due to high heat treatment temperature, such Cr rich precipitation did not occur in the B2 phase.

For the C2 alloy, with Al increasing to 25.4 at %, there are only nanoscale BCC phases in a B2 matrix, with no FCC phase even after heat treatment to 1150°C. The composition in the C2 alloy is homogenous, except Cr, which is segregated to the grain boundaries, Figs. 10 and 11, and with no microscale BCC1 phase (Fig. 6). The matrix composition in the C2 alloy was analysed using SEM-EDS as a function of heat treatment temperature in the C2 alloy, which reveals a slight decrease in Cr content to ~10 at% compared to the design composition. Examining Fig. 21 (c) along the red line demonstrates that the Cr segregation of Cr does not lead to a phase change, consistent with the predictions obtained through Thermo-Calc calculations. The average matrix grain size in the C2 alloy is much smaller than that in the C1 alloy, for all heat treatment temperatures. This grain size was inherited from the as-cast structure, showing important differences in the solidification between the two alloys. Moreover, the nanoscale BCC phase has been identified by TEM with nucleation on the Cr rich precipitates, and then this coarsens with a higher volume fraction at higher heat treatment temperatures until 700°C. But the Cr rich precipitates also disappeared at 1150°C in B2 phase, due to the homogenous distribution of the elements at that temperature.

5.2. Magnetic behaviour as a function of alloy composition and heat treatment

5.2.1. Coercivity

It is well known that the coercivity is very sensitive to grain size variation. In the study, the experimental results observed that the coercivity initially increased with grain size growth. Then, after reaching to the maximum value, it decreased with further increases in grain size for both alloys, especially for C1. Given that there are major differences in the phase structure of the alloys at the different heat treatment temperatures, this suggests that Hc can be influenced by multiple microstructures. H_c is higher at 600°C than at 500°C, but the grain size is larger, which is the opposite of the trend at 700°C and 1150°C. A similar trend has been reported in very fine grained materials [45]. The reason behind this phenomenon is that as the grain size decreases to the nanoscale, each grain adopts a single domain state. In this situation, change in magnetisation cannot easily happen by the movement of domain boundaries, and the coercivity value tends to be high,

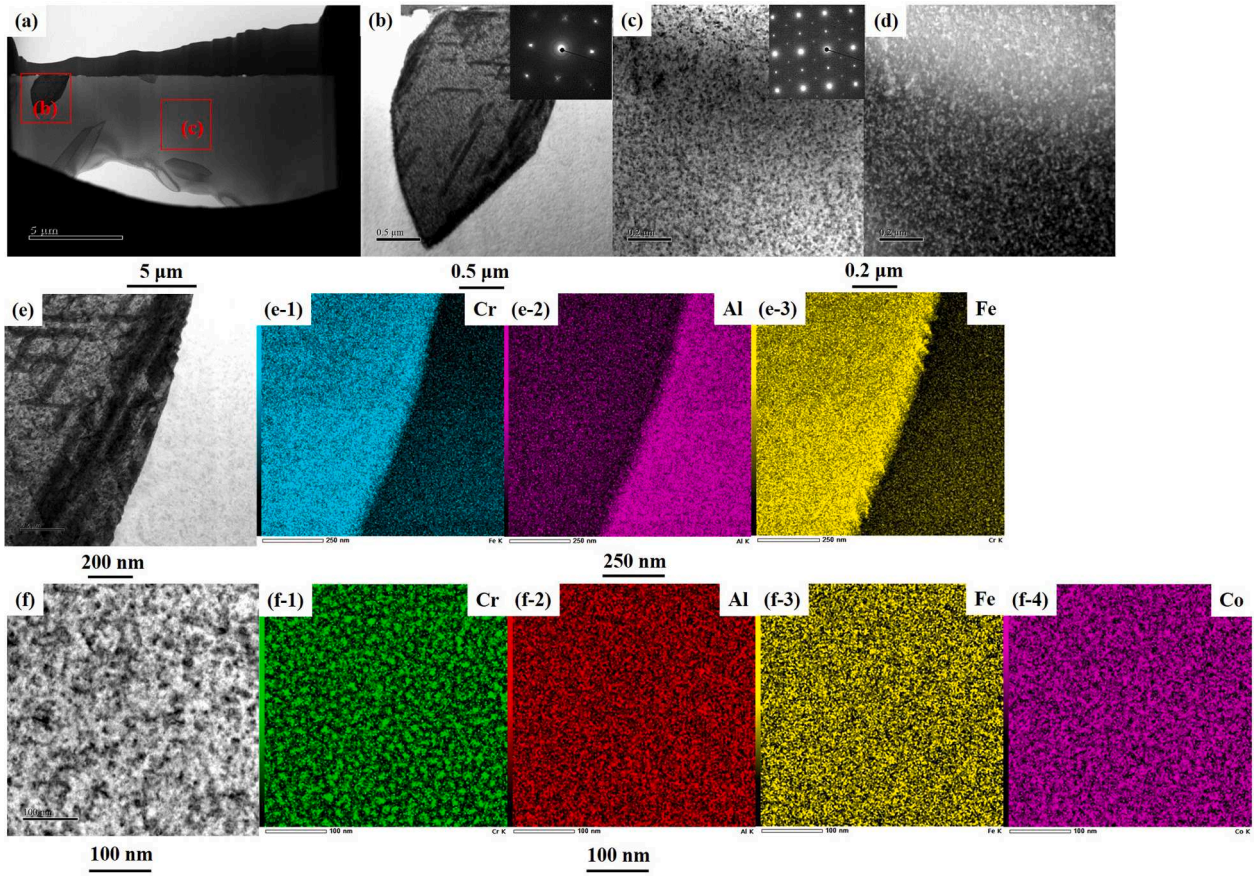

Fig. 13. STEM results from C1: $Co_2FeCr_{0.5}Al_{0.9}$ at 600°C, (a) low magnification bright-field STEM image showing microscale BCC1 phase (dark contrast) and B2 matrix; (b) high magnification bright-field STEM image from red rectangle in (a) shown microscale BCC1 phase with the corresponding diffraction patterns; (c) high magnification bright-field STEM image from red rectangle in (a) shown B2 matrix with nanoscale BCC particles and their corresponding diffraction patterns; (d) Dark-field STEM image from (c); (e) Bright-field STEM image from microscale BCC1 and matrix B2 region with its corresponding EDS maps of (e-1) Cr, (e-2) Al and (e-3) Fe; (f) Bright-field STEM image from B2 matrix and nanoscale BCC region with their corresponding EDS maps of (f-1) Cr, (f-2) Al and (f-3) Fe, (f-4) Co.

demanding a magnetic field larger than the demagnetization field of the single domain state. It has been reported [46] that the presence of nanoscale BCC particles could reduce H_c in a similar way to nanocrystalline phases.

Thus, in this study, there are two empirical relations between the grain size, D, and the coercive field, H_c, have been proposed, Eq. (1) for the nanocrystalline materials and (2) for large grained materials [47]:

$$H_c = aD^6 \tag{1}$$

$$Hc = b/D \tag{2}$$

where a and b are fitting parameters, which can be calculated using the experimental data for H_c and the average grain size, D. Curve-fitting according to equation (1) for the samples found a values of 3.3×10^{-13} in C1, and 4.3×10^{-9} in C2. The fitting parameter b had a value of 6.55×10^5 in C1 and 2.82×10^5 of C2, according to equation (2). Fig. 22 shows the calculated H_c values at 500°C and 600°C using Eq (1), and at 700°C and 1150°C using Eq (2), for the C1 and C2 alloys, which are compared with the experimental data.

For the C1 and C2 at 500°C, 600°C and 700°C, the calculated and measured H_c have similar values. However, for the C1 alloy, the calculated H_c from Eq. (2) at 1150°C are significantly higher than the experimental data. The discrepancy is likely a result of the contribution of the microscale BCC1 phase on the H_c. Therefore, Eq. (2) was modified to take account of the volume fraction and average size of the different phases, giving Eq. (3). In this case, the contribution of the FCC phase was assumed to be the same as the BCC1 phase since the FCC formed from the BCC1.

$$H_{c,\ total} = b'/(V_{BCC1}D_{bcc1}) + b'/(V_{B2}D_{B2}) \tag{3}$$

where V_{BCC} and V_{B2} are the volume fraction values of BCC phase and B2 phase in C1 alloy listed in Fig. 6 (b). The fitting parameter b' is equal to 1.33×10^3 in C1. Thus, Eq. (3) has been used for H_c calculation for the C1 alloy with similar trends to the experimental data. The calculated H_c reduced when taking into account the microscale BCC1 phase effect into Eq (3), which also shows the formation of BCC1 phase is beneficial for the H_c.

The calculation of H_c at 500°C and 600°C fitted well with the experimental data, which proves that the nanoscale BCC phase has an effect on domain wall motion at lower temperature. But this requires that the nanoscale particles are coherent with the matrix. However, in this study, as shown in Table 3, the nanoscale BCC phase at 600°C grows much larger than that at 500°C, with increased volume fraction as well, and this size increases the misfit strain between the nanoscale particles and matrix with effects on the domain wall mobility. Thus, with consideration of the nanoscale BCC phase influence on H_c, the increase in H_c could be explained by the nanoscale particles pinning the domain wall motion for the C1 and C2 alloy. With increasing temperature to 700°C, the nanoscale BCC phase has diminished effect on domain wall motion, due to its larger size. The calculation of H_c at 700°C and 1150°C indicates that H_c is mainly determined by the grain size for C1 and C2 alloys.

Furthermore, the peak in the H_c changed from 600°C in C1 to 700°C in C2, which is associated with the change in microstructure from C1 to

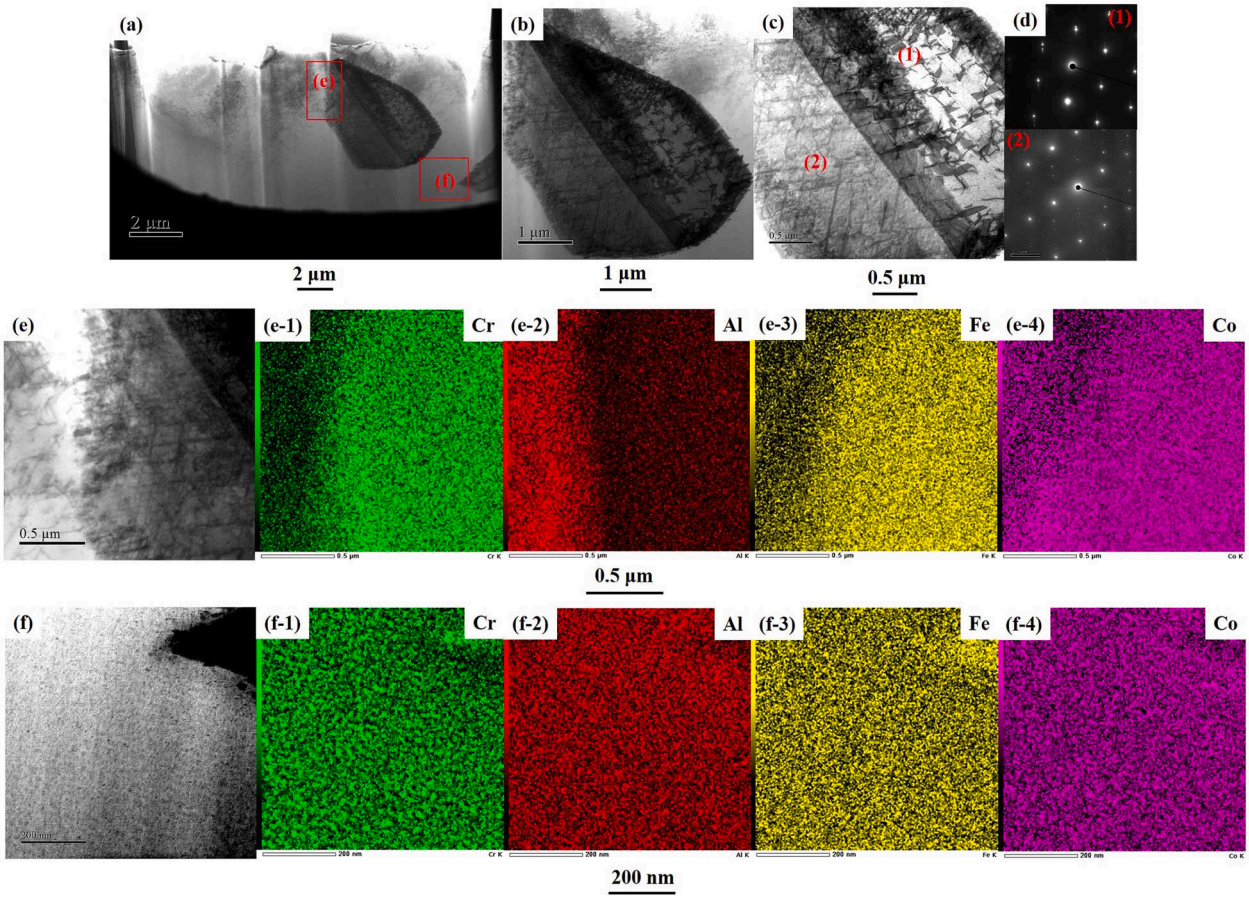

Fig. 14. STEM results from C1: $Co_2FeCr_{0.5}Al_{0.9}$ at 700°C, (a) low magnification bright-field STEM image showing microscale BCC1 phase (dark contrast) and matrix; (b) high magnification bright-field STEM image from red rectangle in (a) shows microscale BCC1 phase; (c) microscale BCC1 phase with the corresponding diffraction patterns shown in (d); (e) Bright-field STEM image from red rectangle in (a) shows microscale BCC1 phase and B2 matrix with its corresponding EDS maps of (e-1) Cr, (e-2) Al and (e-3) Fe, (e-4) Co; (f) Bright-field STEM image from red rectangle in (a) shown B2 matrix and nanoscale BCC region with their corresponding EDS maps of (f-1) Cr, (f-2) Al and (f-3) Fe, (f-4) Co.

C2. For the C1 alloy, as the heat treatment temperature increases from 500°C to 600°C the Cr partitions into the microscale BCC1 phase, which also has a lower Al content, as shown in Fig. 14. This produces weaker ferromagnetic behaviour in the microscale BCC1. However, for the B2 phase, the opposite effect occurred with Cr diffusing out of the BCC1 and Al diffusing in, which is believed to enhance the ferromagnetic behaviour [48,49]. Therefore, these changes could result in a lower volume fraction of nanoscale BCC with lower Cr content in the B2 phase. As a result, the influence of the nanoscale BCC on Hc in C1 is lower, and there is a more rapid transition to the grain size controlled regime than in C2.

5.2.2. *Saturation Magnetisation, M_s*

The saturation magnetization value of each phase in the C1 and C2 alloys is calculated by the equation below [50], considering the different phases:

$$\mathrm{Ms,\ phase} = \frac{n_B \mu_B}{a^3} \tag{4}$$

n_B is the number of Bohr magnetons per unit cell; μ_B is the unit magnetic moment in the supercell, 9.27×10^{-24} Am^2; a is a cubic unit cell edge length, which is measured from the diffraction pattern for each phase. The total M_s values of the C1 and C2 alloys are the combinations of the constituent phases [23], thus:

$$Ms, total = V_{B2}M_{s,B2} + \left(V_{BCC1}M_{s,BCC1} \,/\, V_{FCC}M_{s,FCC}\right) + V_{BCC2}M_{s,BCC2} \tag{5}$$

for C1 alloy and

$$Ms, total = V_{B2}M_{s,B2} + V_{BCC}M_{s,BCC} \tag{6}$$

For the C2 alloy. V_{B2}, V_{BCC}, V_{BCC1}/V_{FCC} are the volume fractions of B2 and BCC phases, and of the BCC1 and FCC phases in C1 alloy, shown in Table 4 and Fig. 5 (b). $M_{s,\ B2}$, $M_{s,\ BCC}$, $M_{s,\ BCC1}/M_{s,\ FCC}$ are the saturation magnetization calculated by Eq (4) for each phase. Fig. 23 shows the experimental and calculated M_s values for the C1 and C2 alloys. The trends for the change in saturation magnetization with temperature are predicted by the model, although there are still gap from the actual values, especially for C1. The predicted M_s of the C1 alloy is higher for all conditions than the measured M_s, which is caused by the complicated phase system in C1 alloy with two types of BCC phases. With a simplified phase system in the C2 alloy, the calculated M_s values are similar to the measured data, especially at 1150°C with nearly the same results. The change of M_s is brought about by the elemental diffusion that occurs during the heat treatments, and the partitioning of the elements in different phases, which affects the lattice constants. The M_s increased from 500°C to 600°C for both C1 and C2 alloys with BCC nanoparticle volume fraction increasing, with expansion of the lattice. The volume fraction of the BCC1 phase in the C1 alloy also increased with a small change in lattice spacing. This is because of the Cr rich precipitation in the B2 phase, with only a few of these regions transformed into BCC nanoparticles at 500°C, shown in Figs. 11 and 16. With increasing heat treatment temperature to 600°C, only the volume fraction of BCC nanoparticles is increased. However, after heat treatment at 700°C, the M_s for both alloys decreased with increase in the lattice spacing for both B2 and BCC phases, which showed that there is more Cr segregated into

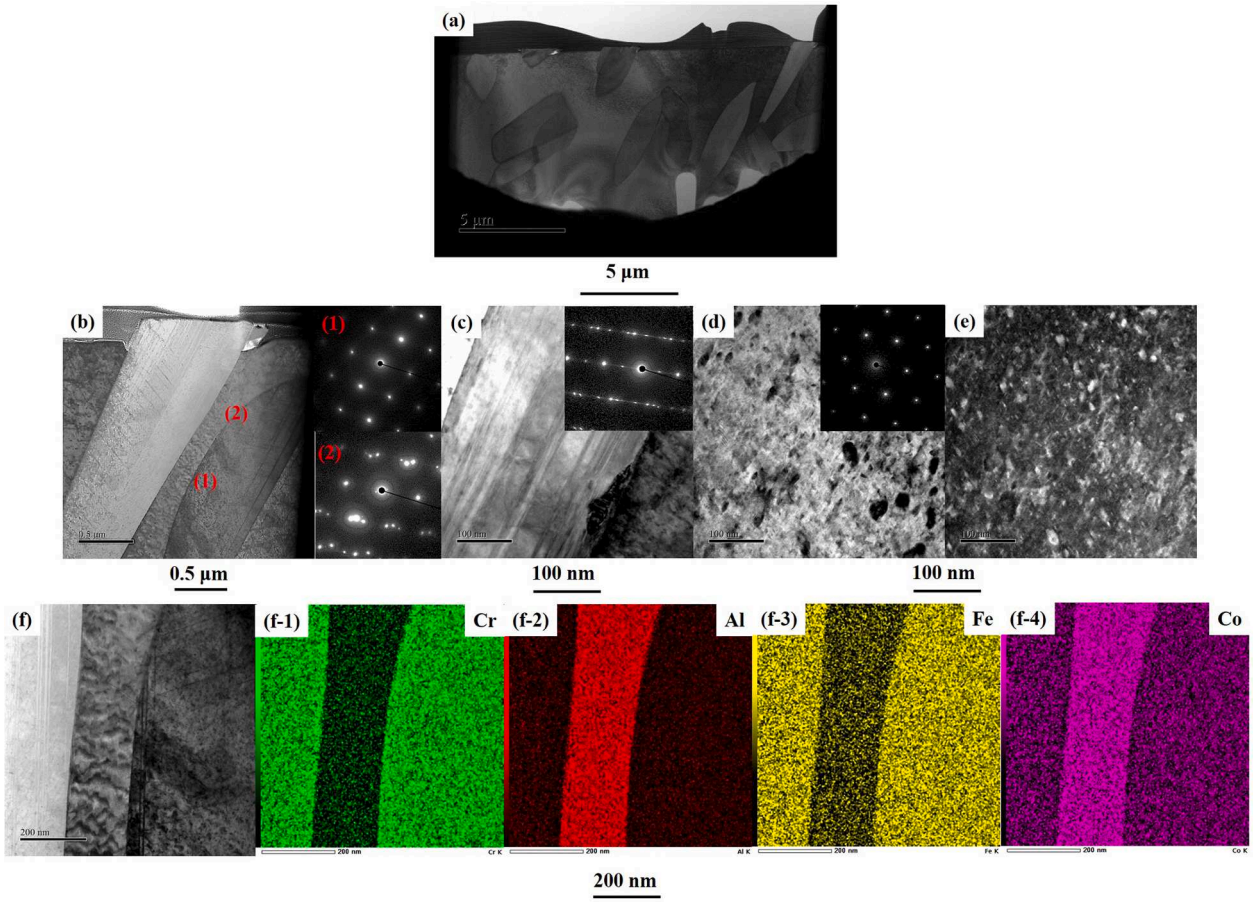

Fig. 15. STEM results from C1: $Co_2FeCr_{0.5}Al_{0.9}$ at 1150°C, (a) low magnification bright-field STEM image showing microscale BCC1 phase (dark contrast) and B2 matrix; (b) high magnification bright-field STEM image showing microscale BCC1 phase with the corresponding diffraction patterns; (c) high magnification bright-field STEM image showing twinning structures in microscale BCC1 phase with the corresponding diffraction patterns; (d) high magnification bright-field STEM image showing B2 matrix with the corresponding diffraction patterns; (e) Dark-field STEM image from (e); (f) Bright-field STEM image from microscale BCC1 phase and B2 matrix region with its corresponding EDS maps of (f-1) Cr, (f-2) Al and (f-3) Fe, (f-4) Co.

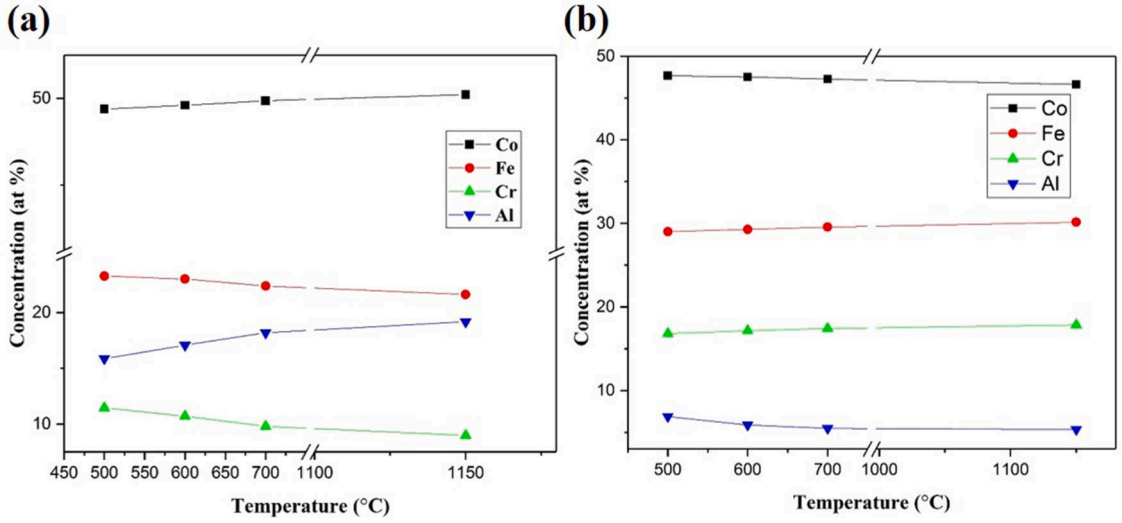

Fig. 16. EDS results from Figs. 11-14 with composition for the B2 matrix and microscale BCC1: (a) B2 matrix, (b) microscale BCC1.

the BCC phase, Cr being an antiferromagnetic element that weakens the saturation magnetization[51]. This effect led to a lower $M_{s,\ BCC}$, which reduced the $M_{s,\ total}$. For the C1 alloy, the $M_{s,\ total}$ reduced more rapidly than for the C2 alloy, due to the weakly ferromagnetic FCC phase being formed from the BCC1 phase. With an increase in the heat treatment temperature to 1150°C, most of the BCC1 phase in the C1 alloy transformed to the FCC phase, which caused a significant reduction in the $M_{s,\ total}$ compared to the C2 alloy with only BCC/B2 phase[52,53]. The $M_{s,}$

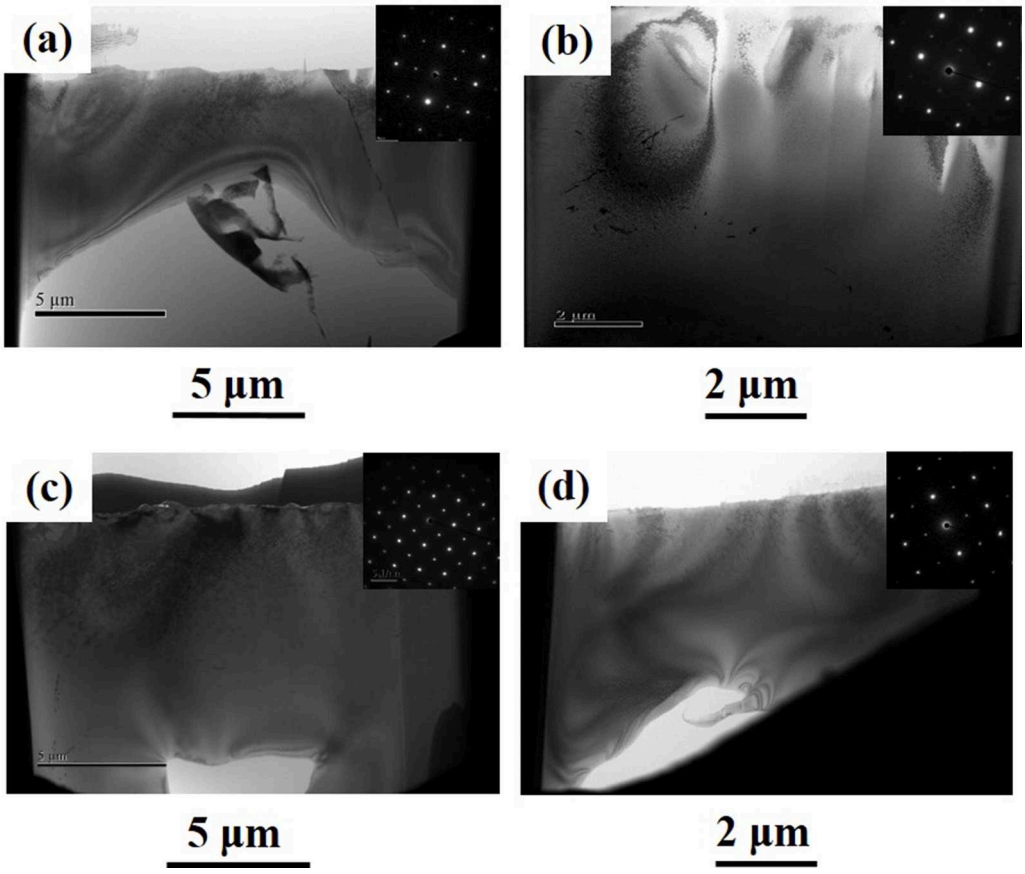

Fig. 17. STEM results from C2: Co2FeCr0.5Al1.2, low magnification Bright-field STEM image with it corresponding diffraction pattern: (a) 500°C of $[011]_{bcc}$; (b) 600°C of $[011]_{bcc}$; (c) 700°C of $[001]_{bcc}$; (d) 1150°C of $[011]_{bcc}$.

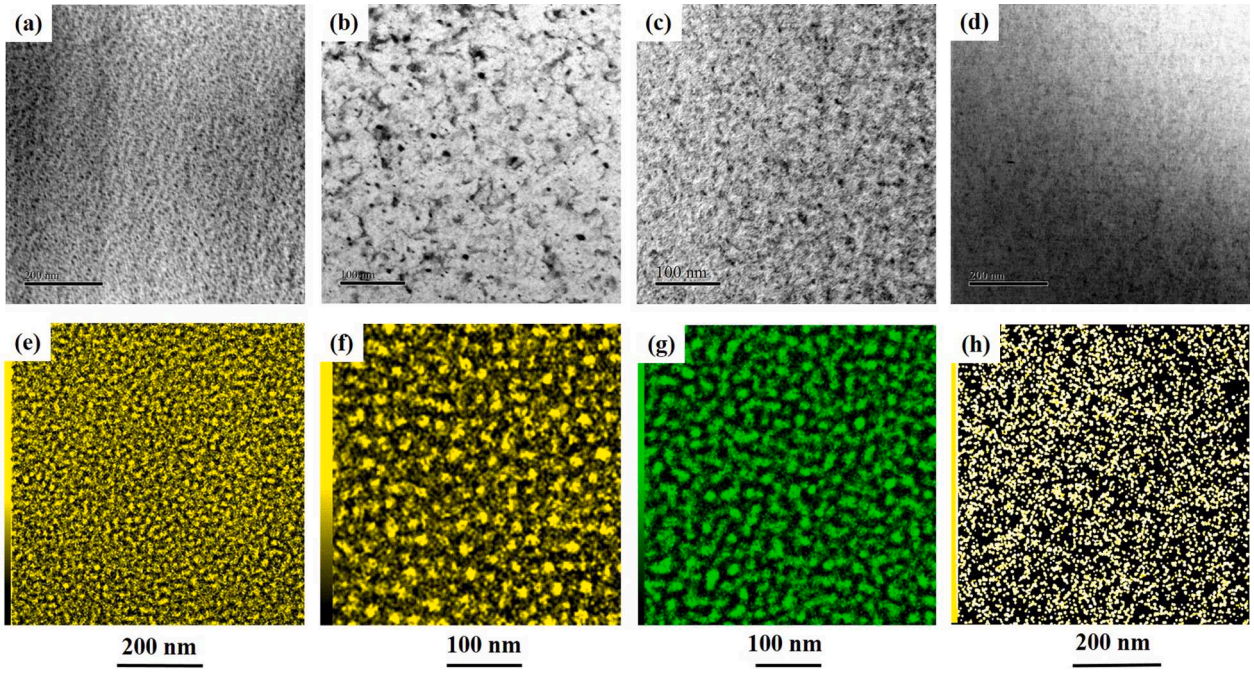

Fig. 18. High magnification Bright-field STEM image with BCC1 nanoparticles and its corresponding STEM-EDS map of Cr from C2; (a) and (e) 500°C; (b) and (f) 600°C; (c) and (g) 700°C; (d) and (h) 1150°C.

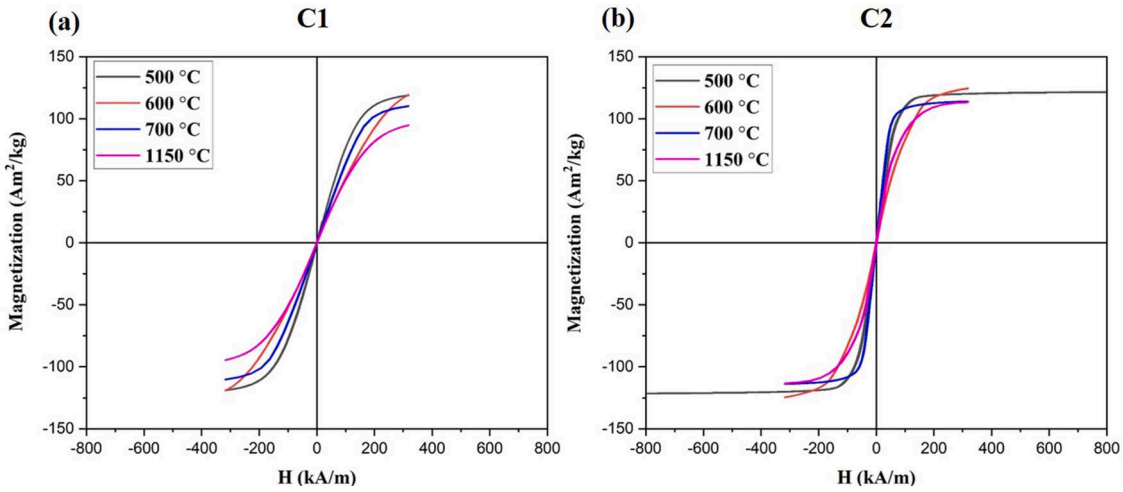

Fig. 19. Magnetization curves showing the hysteresis loops of the studied alloys: (a) C1 alloy; (b) C2 alloy.

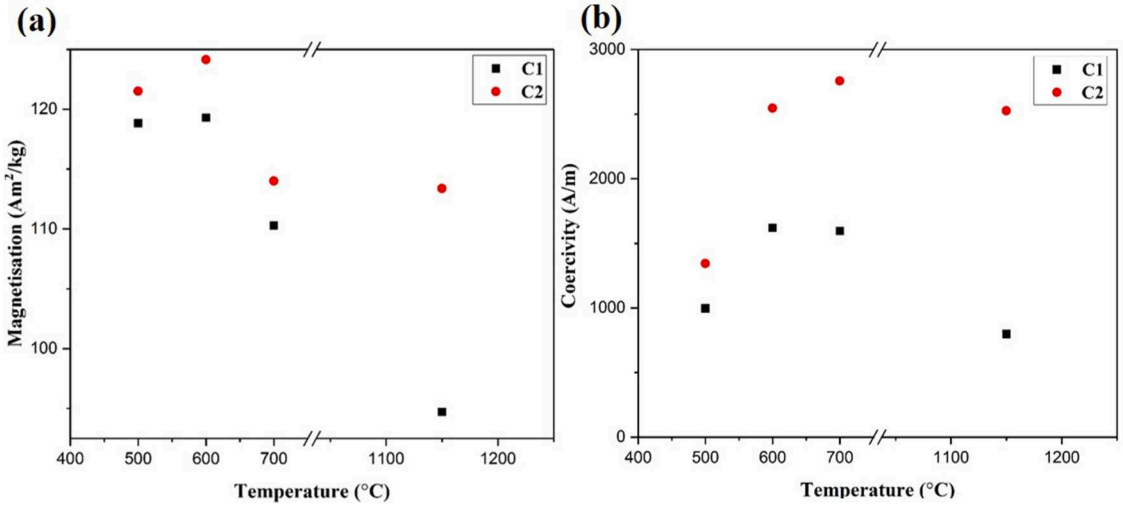

Fig. 20. Measured values of (a) saturation magnetization and (b) coercivity. Each datum is an average of two measurements.

$_{total}$ for the C2 alloy was only slightly reduced at 1150°C due to the nanoscale particles being dissolved into the B2 matrix, with lattice spacing increasing in the matrix. Thus, the results show that the M_s can also be affected by elemental diffusion, controlled through increasing the heat treatment temperatures, which results in a change in the lattice spacing, a similar mechanism to the control of the M_s through the elemental composition[54,55]. The best M_s would be obtained through reducing the misfit between the nanoparticles of the BCC phase and B2 matrix for both C1 and C2 alloys at 600°C. In summary, although the C2 alloy with nanoscale precipitates has a higher saturation magnetization than the C1 alloy for the whole heat treatment process, the C1 alloy with microscale second phase has been found to have better coercivity than the C2 alloy, which is caused by the weaker drag effect on grain boundaries mobility from solute elements and antiferromagnetic segregation into the second phase. For the C1 alloy, the Ms at 500°C and 600°C are nearly similar, with only slightly increasing at 600°C, but at 500°C, the H_c is much less than that at 600°C.

6. Conclusions

Two new soft magnetic multicomponent alloys, $Co_2FeCr_{0.5}Al_x$ (C1: x = 0.9; C2: x = 1.2) have been designed according to our previous research. The microstructural evolution has been studied using XRD, OM, SEM and TEM as a function of heat treatment temperature. The magnetic properties have been derived from VSM magnetometry. The correlation between the microstructure and soft magnetic properties led to the following conclusions:

1 H_c is mainly determined by the grain size of the B2 matrix and the average size of the BCC1/BCC second phase. For both alloys, the coercivity increased with heat treatment temperature up to a peak (600°C for C1 and 700°C for C2) and then decreased with further increase in heat treatment temperature. Below the peak, the coercivity was controlled by the BCC nanoparticles, while above the peak, it was controlled by grain size. The BCC1/ BCC second phase induced an increase in H_c as a result of the resistance to domain wall movement, which weakened the grain coarsening effect on the H_c. However, for the C1 alloy the rapid increase in the grain size of the microscale BCC1 at high heat treatment temperatures from 700°C to 1150°C increased the grain size effect on H_c with improvement of performance.
2 The M_s was mainly influenced by elemental diffusion and partitioning, which increased with increasing Cr rich BCC and BCC1 precipitation, and then decreased with the coarsening of the BCC1/ BCC size. This led to higher contents of antiferromagnetic Cr and increased misfit strains at the interphase boundary.
3 For the C1 alloy, a phase transformation was observed during heat treatment at 700°C and 1150°C, resulting in the conversion of the

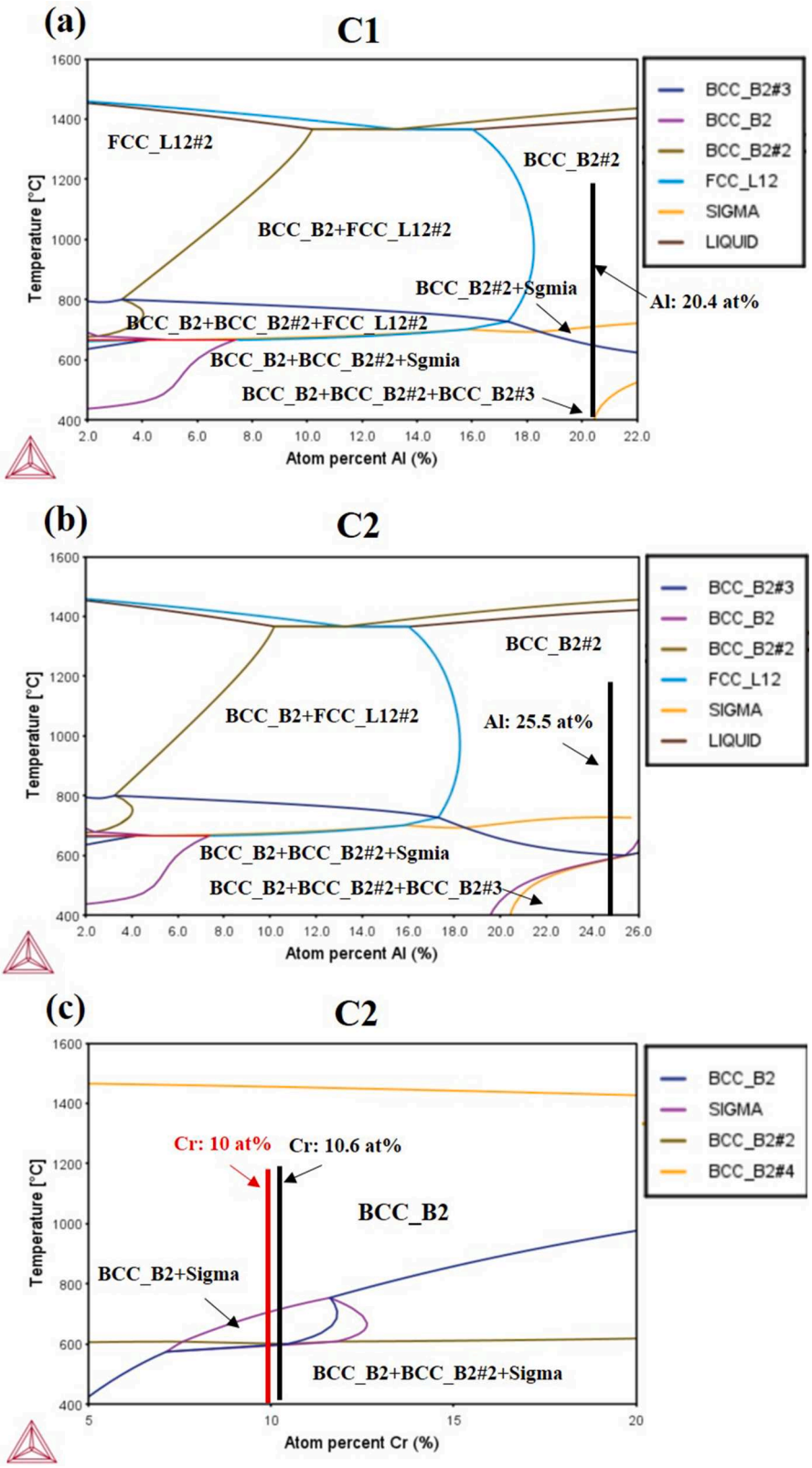

Fig. 21. Calculated phase diagram of C1 and C2 through ThermoCalc: (a) C1 Al system; (b) C2 Al system; (c) C2 Cr system.

microscale BCC1 phase to an FCC phase. This transformation led to a reduction in Ms, due to the weaker ferromagnetic properties of the FCC phase compared to that of the BCC phase. However, when a complete FCC transformation occurred from BCC1 at 1150°C, the H_c decreases significantly, with only a limiting effect from the coherency strains between dual phase boundaries. This effect occurs because the energy required for the displacement of domain walls in the FCC is considerably lower than that in the BCC structure.

Therefore, we conclude that a higher Al content in these alloys is

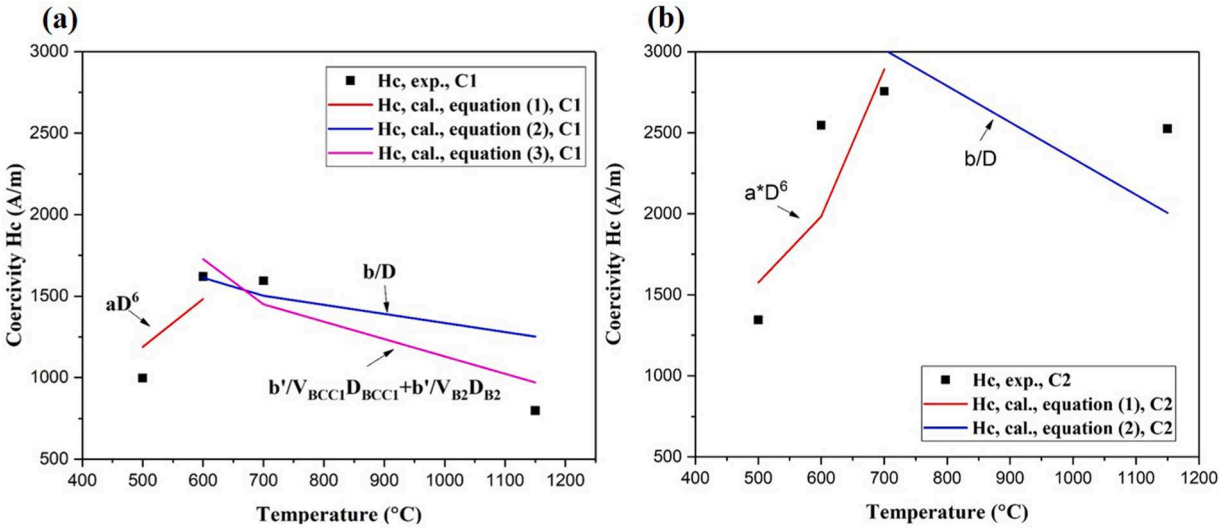

Fig. 22. Calculated and measured H_c for the C1 and C2 alloys as a function of temperature: solid points are the measurement data and lines are the calculated data: (a) C1; (b) C2.

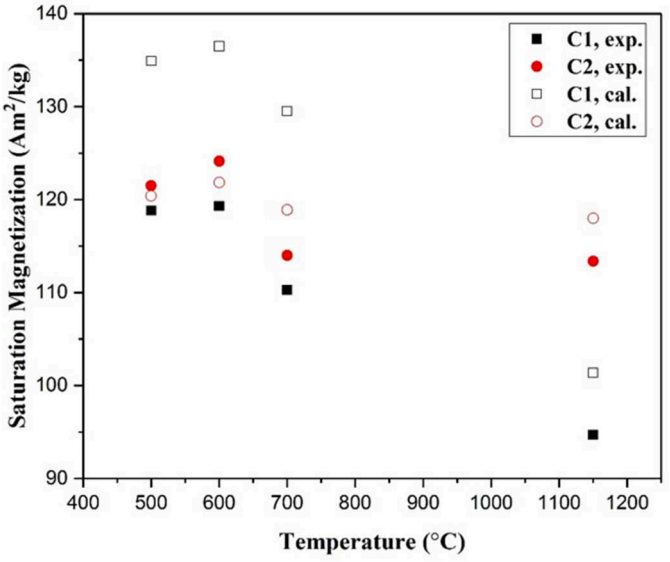

Fig. 23. Calculated and measured M_s for the C1 and C2 alloys as a function of temperatures: solid points are the measurement data and hollow points are the calculated data.

good for the M_s and stabilises BCC/B2 phase, but increases the volume fraction of nanoscale BCC phase which increases H_c. The microscale BCC1 phase, with higher Cr content, slightly reduces the M_s compared to the C2 alloy without BCC1 phase but improves the H_c. However, the BCC1 would transform to FCC at higher heat treatment temperatures with a resultant reduction in M_s. Our current research opens a new window on the design of high-performance soft magnetic alloys using microscale second phases. Control the microstructure, such as second phase particle size, can further improve both M_s and H_c.

Declaration of Competing Interest

The authors declare that they have no known competing financial interests or personal relationships that could have appeared to influence the work reported in this paper.

Acknowledgements

This work is supported by the Engineering and Physical Sciences Research Council (grant number EP/001766/1) as a part of EP/S018107/1, SUSTAIN Future Manufacturing Hub. The authors wish to acknowledge the Henry Royce Institute for Advanced Materials, funded through EPSRC grants EP/R00661X/1 and EP/P02470X/1, for access to the JEOL JEM-F200, and JEOL JEM 7900F.

References

[1] J.E.T. Bistline, Roadmaps to net-zero emissions systems: emerging insights and modeling challenges, Joule 5 (10) (2021) 2551–2563, p.
[2] K.M.J. Barasa, O.O. Akanni, Sustainable energy transition for renewable and low carbon grid electricity generation and supply, 9(2022), p 1–45.
[3] J. Ongena, Y. Ogawa, Nuclear fusion: status report and future prospects, Energy Policy 96 (2021) 770–778, p.
[4] K.T. Chau, W. Li, Overview of electric machines for electric and hybrid vehicles, Int. J. Vehicle Des. 64 (2014) 46–71, p.
[5] M.O A.M.El-Refaie, High specific power electrical machines: a system perspective, CES Trans. Electric. Mach. Syst. (2019) 88–93, 3.1p.
[6] M. Galea. High Performance, Direct Drive Machines for Aerospace Applications, Doctoral dissertation, University of Nottingham, 2013.
[7] D.J. Powell, Modelling of High Power Density Electrical Machines For Aerospace, University of Sheffield, 2004. PhD dissertation.
[8] A. Tenconi, S. Vaschetto, A. Vigliani, Electrical machines for high-speed applications: design considerations and tradeoffs, IEEE Trans. Ind. Electron. 61 (2013) 3022–3029, p.
[9] D. Gerada, A. Mebarki, N.L. Brown, C. Gerada, High speed electrical machines-Technologies, trends and developments, IEEE Trans. Ind. Electron. 61 (2013) 2946–2959, p.
[10] R. Palka, The performance of induction machines, Energies 15 (9) (2022) 3291, p.
[11] W. Yu, W. Hua, Z. Zhang, High-frequency core loss analysis of high-speed, Electronics 10 (2021) 1076, p.
[12] A. Al-timimy, P. Giangrande, M. Degano, M. Galea, Design and losses analysis of a high power density machine for flooded pump applications, IEEE Transac. Industry Appl. 54 (2018) 3260–3270, p.
[13] S. Zurek, Two-Dimensional Magnetisation Problems In Electrical Steels, Cardiff University, 2005. A doctor of philosophy thesis submitted to the wolfson centre for magnetics technology cardiff school of engineering.
[14] Q. Tang, Investigation of Magnetic Properties of Electrical Steel and Transformer Core At High Flux Densities, The University of Manchester, 2015. A PhD thesis submitted to the faculty of engineering and physical sciences, school of electrical and electronic engineering.
[15] N.M. Nik Rozlin, A.M. Alfantazi, Electrochemical properties of electrodeposited nanocrystalline cobalt and cobalt-iron alloys in acidic and alkaline solutions, J. Appl. Electrochem. 43 (7) (2013) 721–734, p.
[16] J.M. Silveyra, P. Xu, V. Keylin, V. DeGeorge, A. Leary, M.E. McHenry, Amorphous and nanocomposite materials for energy-efficient electric motors, J. Electron. Mater. 45 (2016) 219–225.
[17] T. Clark, S.N. Mathaudhu, Microstructure and magnetic properties of dilute nanocrystalline Fe-Si prepared by high energy ball milling, J. Magn. Magn. Mater. 484 (2019) 350–355, p.

[18] K. Senda, M. Namikawa, Y. Hayakawa, Electrical steels for advanced automobiles-core materials for moters, generators and high-frequency reactors, JEF Tech. Rep. 4 (2004) 67–73, p.
[19] T. Borkar, B. Gwalani, D. Choudhuri, C.V Mikler, C.J. Yannetta, X. Chen, R. V Ramanujan, M.J. Styles, M.A. Gibson, R. Banerjee, A combinatorial assessment of $AlxCrCuFeNi_2$ ($0 \leq x \leq 1.5$) complex concentrated alloys: Microstructure, microhardness, and magnetic properties, Acta Mater. 116 (2016) 63–76, p.
[20] Y. Zhang, T.T. Zuo, Y.Q. Cheng, P.K. Liaw, High-entropy alloys with high saturation magnetization, electrical resistivity and malleability, Sci. Rep. 3 (2013) 1455.
[21] P. Li, A. Wang, C.T. Liu, A ductile high entropy alloy with attractive magnetic properties, J. Alloys Compd. 694 (2017) 55–60, p.
[22] C. Jung, K. Kang, A. Marshal, K. Gokuldoss, J. Seol, H. Mo, P. Choi, Effects of phase composition and elemental partitioning on soft magnetic properties of AlFeCoCrMn high entropy alloys, 171 (2019), p31-39.
[23] Y. Zhang, T.T Zuo, Z. Tang, M.C. Gao, K.A. Dahmen, P.K. Liaw, Z.P. Lu, Microstructures and properties of high-entropy alloys, Prog. Mater. Sci. 61 (2014) 1–93, p.
[24] Y. Zhang, T. Ting, Z. Tang, M.C. Gao, K.A. Dahmen, P.K. Liaw, Z. Ping, Progress in materials science microstructures and properties of high-entropy alloys, Prog. Mater. Sci. 61 (2013) 1–93, p.
[25] Y. Zhang, T. Zuo, Y. Cheng, P.K. Liaw, High-entropy alloys with high saturation magnetization, Electric. Resist. Malleab. Sci. Rep. 3 (2013) 1455.
[26] Y.F. Ye, Q. Wang, J. Lu, C.T. Liu, Y. Yang, High-entropy alloy: challenges and prospects, Mater. Today 19 (2016) 349–362, p.
[27] H. Chou, Y. Chang, S. Chen, J. Yeh, Microstructure, thermophysical and electrical properties in Al x CoCrFeNi ($0 \leq x \leq 2$) high-entropy alloys, Mater. Sci. Eng. B 163 (2009) 184–189, p.
[28] T. Yang, S. Xia, S. Liu, C. Wang, S. Liu, Y. Zhang, J. Xue, S. Yan, Y. Wang, A Effects of AL addition on microstructure and mechanical properties of AlxCoCrFeNi High-entropy alloy, Mater. Sci. Eng. A. 648 (2015) 15–22, p.
[29] R.F.D.A. Cardoso, L. Brandao, M.A.D. Cunha, Influence of grain size and additions of Al And Mn on the magnetic properties of non-oriented electrical steels with 3 wt. (%) Si, Mater. Res. 11 (2008) 51–55, p.
[30] B.T. Borkar, V. Chaudhary, B. Gwalani, D. Choudhuri, C.V. Mikler, V. Soni, T. Alam, R.V. Ramanujan, R. Banerjee, A combinatorial approach for assessing the magnetic properties of high entropy alloys: role of Cr in AlCoxCr1-xFeNi, Adv. Eng. Mater. 19 (2017), 1700048 p.
[31] T.T. Zuo, S.B. Ren, P.K. Liaw, Y. Zhang, Processing effects on the magnetic and mechanical properties of FeCoNiAl0.2Si0.2 high entropy alloy, Int. J. Mineral Metall. and Marter. 20 (2013) 549–555, p.
[32] R. Wei, H. Sun, C. Chen, J. Tao, F. Li, Formation of soft magnetic high entropy amorphous alloys composites containing in situ solid solution phase, J. Magn. Magn. Mater. 449 (2018) 63–67, p.
[33] R. Wei, H. Sun, C. Chen, Z. Han, F. Li, Effect of cooling rate on the phase structure and magnetic properties of Fe26.7Co28.5Ni28.5Si4.6B8.7P3, J. Magn. Magn. Mater 435 (2017) 184–186, p.
[34] M. Tsai, J. Yeh, High-Entropy Alloys : A Critical Review, Mater. Res. Lett. 2 (2014) 107–123, p.
[35] V. Chaudhary, V. Soni, B. Gwalani, R.V Ramanujan, R. Banerjee, Scripta materialia influence of non-magnetic Cu on enhancing the low temperature magnetic properties and curie temperature of FeCoNiCrCu(x) high entropy alloys, Scr. Mater. 182 (2020) 99–103, p.
[36] Y. Ma, Q. Wang, X.Y. Zhou, J.M. Hao, B. Gault, Q.Y. Zhang, C. Dong, T.G. Nieh, A novel soft-magnetic B2-based multiprincipal-element alloy with a uniform distribution of coherent body-centered-cubic nanoprecipitates, Adv. Mater. 33 (2021), 2006723.
[37] L. Han, F. Maccari, I.R. Souza Filho, N.J. Peter, Y. Wei, B. Gault, O. Gutfleisch, Z. Li, D. Raabe, A mechanically strong and ductile soft magnet with extremely low coercivity, Nature 608 (2022) 310–316.
[38] M.E. Mchenry, D.E. Laughlin, Nanoscale mateirals development for future magnetic applications, Acta Mater. 48 (2000) 223–238, p.
[39] C. Jung, K. Kang, A. Marshal, K.G. Pradeep, J.B. Seol, H.M Lee, P.P. Choi, Effects of phase composition and elemental partitioning on soft magnetic properties of AlFeCoCrMn high entropy alloys, Acta Mater. 171 (2019) 31–39, p.
[40] K. Suzuki, A. Makino, N. Kataoka, A. Inoue, T. Masumoto, High Saturation Magnetization and soft magnetic properties of bcc Fe-Zr-B and Fe-Zr-B-M alloys with nanaoscale grain size, Mater. Trans. JIM 32 (1991) 93–102, p.
[41] Y. Xueqian, L. Guizhong, B. Yufeng, D. Xintao, G. Jingjie, Influence of gradual replacement of aluminum for copper in FeCrCoNiCu alloys Einfluss des graduellen Austausches von Kupfer durch Aluminium in FeCrCoNiCu-Legierungen, Materialwissenschaft und Werkstofftechnik 49 (2018) 1373–1380, p.
[42] N.A. Morley, B. Lim, J. Xi, A. Quintana-Nedelcos, Z. Leong, Magnetic properties of the complex concentrated alloy system CoFeNi0.5Cr0.5Alx, Sci. Rep. 10 (2020) 14506.
[43] S.Y. Chen, X. Yang, K.A. Dahmen, P.K. Liaw, Y. Zhang, Microstructures and crackling noise of AlxNbTiMoV high entropy alloys, Entropy 16 (2014) 870–884.
[44] W.R. Wang, W.L. Wang, S.C. Wang, Y.C. Tsai, C.H. Lai, J.W. Yeh, Effects of Al addition on the microstructure and mechanical property of AlxCoCrFeNi high-entropy alloys, Intermetallics 26 (2012) 44–51.
[45] J.S. Lee, J.M. Cha, H.Y. Yoon, J. Lee, Y.K. Kim, Magnetic multi-granule nanoclusters : A model system that exhibits universal size effect of magnetic coercivity, Nat. Publ. Gr. (n.d.) 1–7. doi:10.1038/srep12135.
[46] H. Yang, J. Li, T. Guo, W. Yi, W. Hongchao, K. Jun, Fully Recrystallized Al0.5CoCrFeNi High-Entropy Alloy Strengthened by Nanoscale Precipitates, Met. Mater. Int. 25 (2019) 1145–1150, p.
[47] H. Sepehri-Amin, T. Ohkubo, M. Gruber, T. Schrefl, K. Hono, Sciencedirect micromagnetic simulations on the grain size dependence of coercivity in anisotropic Nd-Fe-B sintered magnets, Scr. Mater. 89 (2014) 29–32, p.
[48] D.E. Okpalugo, J.G. Booth, C.A. Faunce, Onset of ferromagnetism in 3d-substituted FeAl alloys. I. Ti, V and Cr substitutions, J. Phys. F Metal. Phys. 15 (1985) 681, p.
[49] G. Acheunert, O. Heinonen, R. Hardeman, A. Lapicki, M. Gubbins, R.M. Bowman, A review of high manetic moment thin films for mcroscale and nanotechnology applications, Appl. Phys. Rev. 3 (2016), 011301.
[50] G. Acheunert, O. Heinonen, R. Hardeman, A. Lapicki, M. Gubbins, R.M. Bowman, A review of high manetic moment thin films for mcroscale and nanotechnology applications, Appl. Phys. Rev. 3 (2016), 011301.
[51] V. Chaudhary, B. Gwalani, V. Soni, R.V. Ramanujan, R. Banerjee, Influence of Cr Substitution and Temperature on Hierarchical Phase Decomposition in the AlCoFeNi High Entropy Alloy, Sci. Rep. 8 (2018) 1–12, p.
[52] V.S. Hariharan, A. Karati, T. Parida, R. John, D.A. Babu, B.S. Murty, Effect of Al addition and homogenization treatment on the magnetic properties of CoFeMnNi high-entropy alloy, J. Mater. Sci. 55 (2020) 17204–17217, p.
[53] J. Cieslak, J. Tobola, M. Reissner, Intermetallics The effect of bcc/fcc phase preference on magnetic properties of AlxCrFeCoNi high entropy alloys, Intermetallics 118 (2019), 106672 p.
[54] J.J. Wang, Z.D. Kou, S. Fu, S.S. Wu, S.N. Liu, M.Y. Wang, D. Wang, S. Lan, H. Hahn, T. Feng, Microstructure and magnetic properties evolution of Al/CoCrFeNi nanocrystalline high-entropy alloy composite, Rare Met. 41 (2022) 2038–2046, p.
[55] K. Akedo, T. Ishizaki, K. Yatsugi, Structural and magnetic properties of size-controlled Fe-Ni nanoparticles synthesized by diffusing Fe atoms into preformed Ni nanoparticles, J. Nanopart. Res. 23 (2021) 1–12, p.